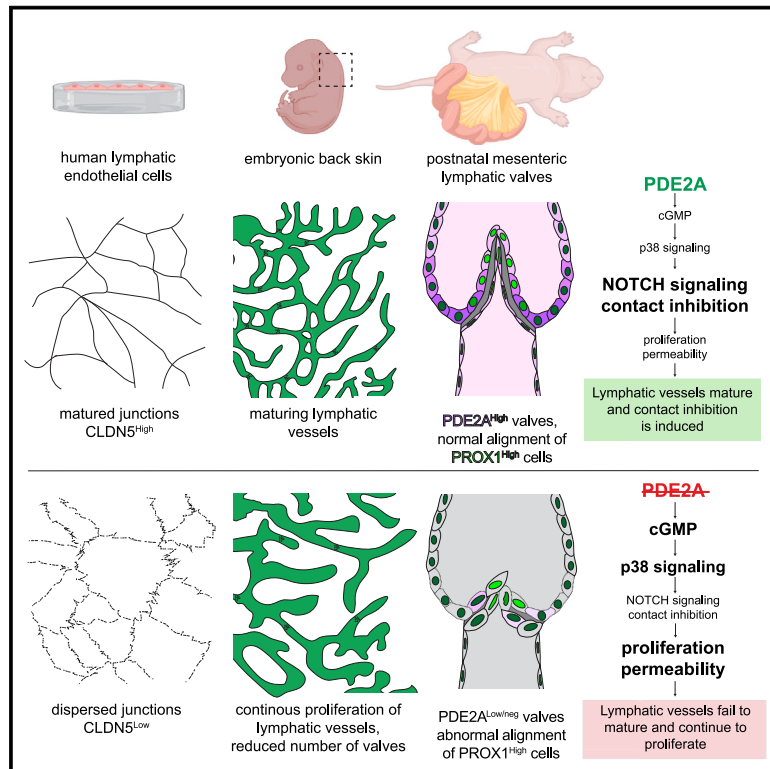# The phosphodiesterase 2A controls lymphatic junctional maturation via cGMP-dependent notch signaling

Graphical abstract

Authors

Claudia Carlantoni, Leon M.H. Liekfeld,
Sandra A. Hemkemeyer, ...,
Viacheslav O. Nikolaev,
Thomas Renné, Maike Frye

Correspondence

m.frye@uke.de

In brief

Carlantoni et al. demonstrate that loss of lymphatic PDE2A prevents the formation of mature lymphatic junctions, and this results in continuous proliferation and lymphatic dysfunction in human primary cells and mouse models. Lymphatic PDE2A exerts its function by controlling p38 and NOTCH signaling via cGMP modulation.

Highlights

- The phosphodiesterase 2A is enriched in lymphatic endothelial cells

- Loss of lymphatic PDE2A prevents contact inhibition and junctional maturation

- PDE2A controls p38 and Notch signaling in a cGMP-dependent manner

- Postnatal mesenteric lymphatic valves are defective in the absence of PDE2A

CellPress

Article

The phosphodiesterase 2A controls lymphatic junctional maturation via cGMP-dependent notch signaling

Claudia Carlantoni,[1,2,12] Leon M.H. Liekfeld,[1,12] Sandra A. Hemkemeyer,[1,2] Danny Schreier,[1] Ceren Saygi,[3] Roberta Kurelic,[4] Silvia Cardarelli,[5] Joanna Kalucka,[6] Christian Schulte,[2,7] Manu Beerens,[1,2] Reiner K. Mailer,[1] Tilman E. Schäffer,[8] Fabio Naro,[5] Manuela Pellegrini,[5,9] Viacheslav O. Nikolaev,[2,4] Thomas Renné,[1,10,11] and Maike Frye[1,2,13,*]

[1]Institute of Clinical Chemistry and Laboratory Medicine, University Medical Center Hamburg-Eppendorf, Hamburg 20246, Germany
[2]German Centre of Cardiovascular Research (DZHK), Partner Site Hamburg/Luebeck/Kiel, Hamburg, Germany
[3]Bioinformatics Core, University Medical Center Hamburg-Eppendorf, Hamburg 20246, Germany
[4]Institute of Experimental Cardiovascular Research, University Medical Center Hamburg-Eppendorf, Hamburg 20246, Germany
[5]DAHFMO-Unit of Histology and Medical Embryology, Sapienza University of Rome, 00161 Rome, Italy
[6]Department of Biomedicine, Aarhus University, Aarhus, Denmark
[7]Department of Cardiology, University Heart & Vascular Center Hamburg, University Medical Center Hamburg-Eppendorf, Hamburg, Germany
[8]Institute of Applied Physics, University of Tuebingen, 72076 Tuebingen, Germany
[9]Institute of Biochemistry and Cell Biology, IBBC-CNR, Campus A. Buzzati Traverso, Monterotondo Scalo, Rome 00015, Italy
[10]Center for Thrombosis and Hemostasis (CTH), Johannes Gutenberg University Medical Center, Mainz, Germany
[11]Irish Centre for Vascular Biology, School of Pharmacy and Biomolecular Sciences, Royal College of Surgeons in Ireland, Dublin, Ireland
[12]These authors contributed equally
[13]Lead contact
*Correspondence: m.frye@uke.de
https://doi.org/10.1016/j.devcel.2023.12.002

SUMMARY

The molecular mechanisms by which lymphatic vessels induce cell contact inhibition are not understood. Here, we identify the cGMP-dependent phosphodiesterase 2A (PDE2A) as a selective regulator of lymphatic but not of blood endothelial contact inhibition. Conditional deletion of *Pde2a* in mouse embryos reveals severe lymphatic dysplasia, whereas blood vessel architecture remains unaltered. In the absence of PDE2A, human lymphatic endothelial cells fail to induce mature junctions and cell cycle arrest, whereas cGMP levels, but not cAMP levels, are increased. Loss of PDE2A-mediated cGMP hydrolysis leads to the activation of p38 signaling and downregulation of NOTCH signaling. However, DLL4-induced NOTCH activation restores junctional maturation and contact inhibition in PDE2A-deficient human lymphatic endothelial cells. In postnatal mouse mesenteries, PDE2A is specifically enriched in collecting lymphatic valves, and loss of *Pde2a* results in the formation of abnormal valves. Our data demonstrate that PDE2A selectively finetunes a crosstalk of cGMP, p38, and NOTCH signaling during lymphatic vessel maturation.

INTRODUCTION

Dynamic remodeling of endothelial cell (EC)-cell contacts provides the prerequisite for initial sprout formation at the onset of lymphatic and blood vascular development.[1,2] At later stages, cell junctions mature, and vessel integrity is established to form the endothelial barrier between the lymph or blood and the surrounding tissue.[3]

ECs exit their cell cycle and undergo cell contact inhibition upon confluency. Formation of stable junctions in blood ECs (BECs) induces intracellular signals that restrain the capacity of the cells to respond to proliferative signals.[4] Furthermore, vascular endothelial (VE)-cadherin-mediated signaling,[5,6] YES-

associated protein 1 (YAP1),[7] and NOTCH signaling[8] have been shown to control BEC contact inhibition. Although this process has been extensively studied in BECs, little is known about the molecular mechanisms by which contact inhibition is induced during development of the lymphatic vasculature, despite its key role in fluid homeostasis, fat absorption, and immune cell transport and in diseases, such as lymphedema, cancer, and immunological dysfunction.[9]

Dynamics of the endothelial barrier are further controlled by the combined action of intracellular signals, such as TIE, NOTCH, FOXC2, GTPase, and cyclic nucleotide signaling,[10–13] and extracellular factors, such as fluid mechanics and matrix stiffness.[14,15] To this end, lymphatic ECs (LECs) and BECs are equipped with
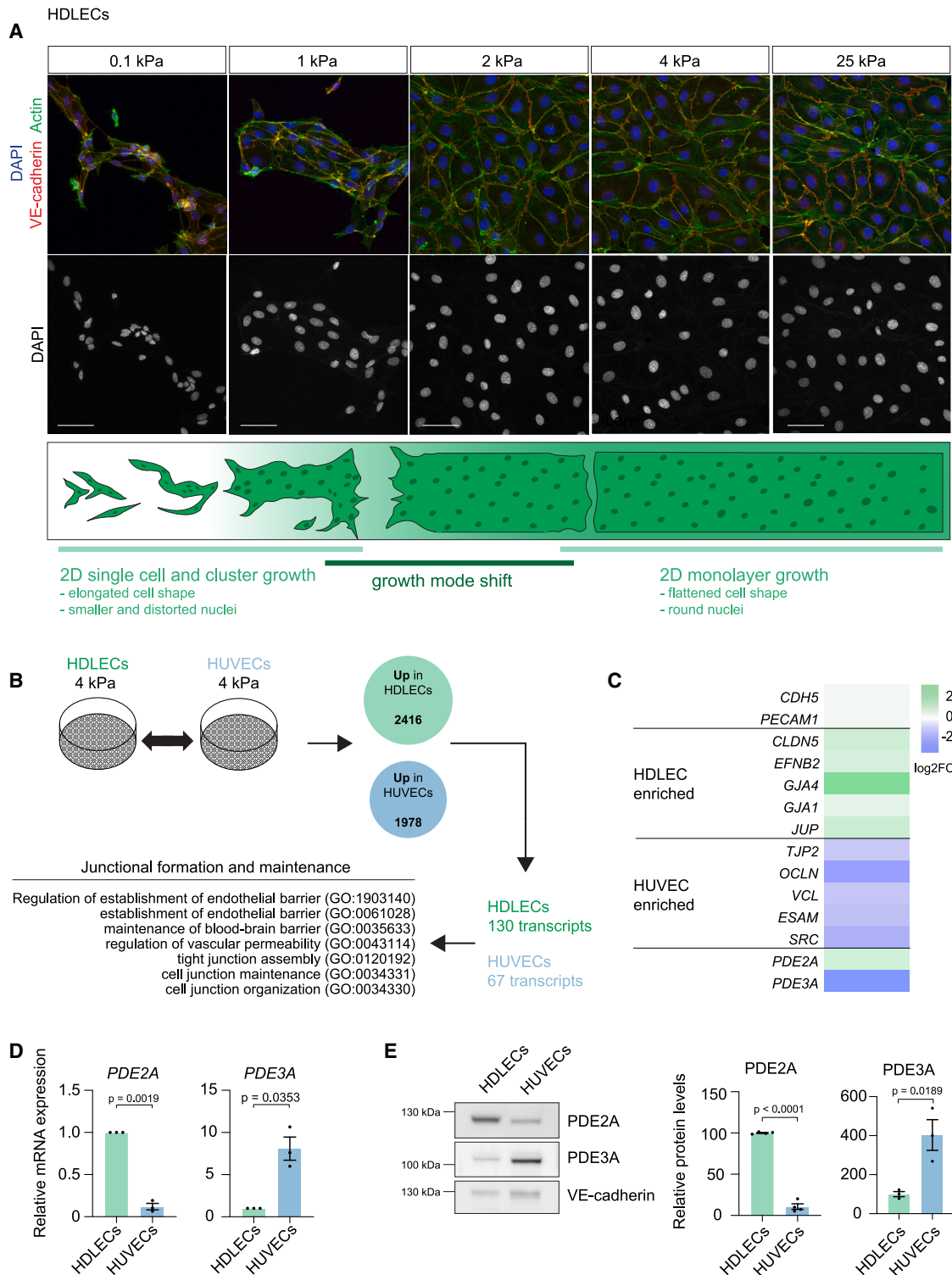
Figure 1. PDE2A is enriched in lymphatic endothelial cells

(A) Representative immunofluorescence staining of HDLECs, grown on polyacrylamide stiffness substrates ranging from 0.1 to 25 kPa, using an antibody against VE-cadherin (red), phalloidin (green, to visualize actin), and DAPI (blue). Single channel images for DAPI are shown. Scale bars, 50 μm.

(B) Global transcriptome analysis of HDLECs and HUVECs grown on physiological 4 kPa stiffness substrates. Number of enriched transcripts (n = 3 biological replicates) in HDLECs and HUVECs are shown. Among these, differentially regulated transcripts associated with Gene Ontology (GO) terms of junctional formation and maintenance were selected.

(legend continued on next page)

a plethora of similar molecules, which can have multifaceted roles in different EC types and developmental stages. For example, deletion of VE-cadherin (*Cdh5*) is dispensable for junctional maintenance of mature blood vessels in mouse skin and brain,[16] mature mouse dermal lymphatic vessels (LVs),[17] and cell-cell junctions of human dermal LECs (HDLECs).[18] Recent findings further showed that the receptor tyrosine kinase EphB4 selectively regulates the junctional integrity of postnatal and adult lymphatics[18] and adult cardiac capillaries.[19]

Cyclic nucleotide phosphodiesterases (PDEs) comprise a superfamily of metallophosphohydrolases that specifically hydrolyze the second messenger cyclic adenosine monophosphate (cAMP) and/or cyclic guanosine monophosphate (cGMP) to AMP and GMP, respectively. In mammals, the PDE protein family can be divided into three groups depending on their substrate selectivity: cAMP-specific, cGMP-specific, and PDEs with dual specificity. Among the latter category, the cAMP/cGMP-converting enzyme PDE2 is the only cAMP-hydrolyzing PDE, which is allosterically activated by cGMP. Due to this unique role, PDE2 has been suggested to play a role at the center of the crosstalk between cGMP and cAMP signaling.[20] In BECs, relative expression levels of phosphodiesterase 2A (PDE2A) and another PDE, the cGMP-inhibited PDE3A, have been shown to regulate blood endothelial junctions,[21,22] but the function of PDE2A in LECs is not known.

Here, we studied the role of the PDE2A in lymphatic development and junctional integrity using conditional *Cre/loxP*-mediated gene deletion in mice and corresponding analysis in primary human LECs. We found that mouse embryos developed severe lymphatic dysplasia upon the deletion of endothelial *Pde2a*, whereas large blood vessels were unaltered. In the absence of PDE2A, human LECs failed to induce mature CLDN5^{High} junctions and cell cycle arrest. Consistent with defective junctional maturation, loss of endothelial *Pde2a* expression in mice interfered with lymphatic maturation and blocked contact inhibition at later stages during embryonic development. During postnatal development, PDE2A was enriched in lymphatic valves of collecting and large pre-collecting mesenteric LVs , and lymphatic-specific deletion of *Pde2a* resulted in abnormal lymphatic valves. Unexpectedly, lymphatic cGMP levels, but not cAMP levels, were increased in PDE2A-deficient LECs. Intriguingly, dysregulated lymphatic cGMP was associated with increased p38 phosphorylation and reduced NOTCH signaling, whereas exogenous activation of NOTCH via its ligand Delta-like 4 (DLL4) was able to restore CLDN5^{High} expression and junctional maturation. Our data uncover a selective mechanism of lymphatic maturation via the previously unappreciated PDE2A/cGMP/p38/NOTCH axis.

RESULTS

Expression of the PDE2A is enriched in LECs
During embryonic development, lymphatic endothelial progenitors and venous ECs within the cardinal vein experience extra-

cellular matrix (ECM) stiffness around 4 kPa.[23] They are tightly attached to the underlying basement membrane and show a flattened, spread-out monolayer morphology, whereas in a soft microenvironment (0.2 kPa), lymphatic endothelial progenitors preferably migrate.[23] Similarly, human LECs in culture switch from a migratory, spindle shape phenotype on very soft substrates (0.1 kPa) to a flattened morphology with the capacity to form a continuous monolayer on moderate stiffness substrates (4 kPa) (Figure 1A).

To identify potential selective regulators of lymphatic and BEC junction formation and vessel maturation in a physiological stiffness environment that reinforces junctional integrity, we performed global transcriptome analysis (RNA sequencing [RNA-seq]) of lymphatic (HDLECs) and venous ECs (human umbilical vein ECs [HUVECs]) grown on 4 kPa stiffness substrates. RNA-seq analysis revealed cell type-specific upregulation of 2,416 and 1,978 transcripts in HDLECs and HUVECs, respectively (log$_2$-fold change >0.5 or <−0.5) (Figure 1B). Within these upregulated transcripts, we identified 130 HDLEC transcripts and 67 HUVEC transcripts that were annotated to Gene Ontology (GO) terms related to endothelial junction formation and maintenance (Figure 1B).

The junctional molecules VE-cadherin (*CDH5*) and CD31 (*PECAM1*) were not differentially expressed between both cell types *in vitro*. However, mRNA levels of claudin 5 (*CLDN5*) and EphrinB2 (*EFNB2*), which we have previously identified to regulate LEC junctions,[18] were upregulated in HDLECs (Figure 1C). Notably, strongly enriched transcripts included the PDEs *PDE2A* (upregulated in HDLECs) versus *PDE3A* (upregulated in HUVECs) (Figure 1C), of which the relative expression levels have been shown to regulate blood endothelial permeability.[21] Quantitative real-time PCR analysis of HDLECs and HUVECs grown for 72 h confirmed RNA-seq findings and showed an 8.3-fold decrease of *PDE2A* and an 8.1-fold increase of *PDE3A* mRNA levels in HUVECs compared with HDLECs (Figure 1D).

Similarly, PDE2A and PDE3A showed inverse protein expression levels in HDLECs compared with HUVECs (Figure 1E). We therefore sought to analyze if enriched expression of PDE2A in LECs could reflect a unique role of this PDE for regulation of lymphatic junctions compared with venous blood endothelial junctions.

Endothelial-specific deletion of *Pde2a* results in severe dysplasia of the embryonic lymphatic vasculature
Consistent with our human data, single-cell RNA-seq (scRNA-seq) data from the Tabula muris database[24] show enrichment of *Pde2a* gene expression in LECs. Using literature-curated marker genes of cell phenotypes, we exemplarily identified an LEC cluster in mouse lungs (Figure S1A), which showed a high expression of *Pde2a* in LECs and a low expression of *Pde3a* in pulmonary ECs with a main presence in non-EC types (Figures S1B and S1C). We therefore focused on the analysis of PDE2A function in LECs *in vivo*.

(C) Heatmap of selected enriched transcripts in HDLECs and HUVECs.

(D) Relative mRNA expression levels of *PDE2A* and *PDE3A* in HDLECs and HUVECs from n = 3 independent experiments. Mean ± SEM, p value: one-sample t test.

(E) Western blot analysis and quantification of PDE2A (n = 4 independent experiments) and PDE3A (n = 3 independent experiments) expression in HDLECs and HUVECs. VE-cadherin was used as endothelial loading control. Mean ± SEM, p value: unpaired Student's t test.
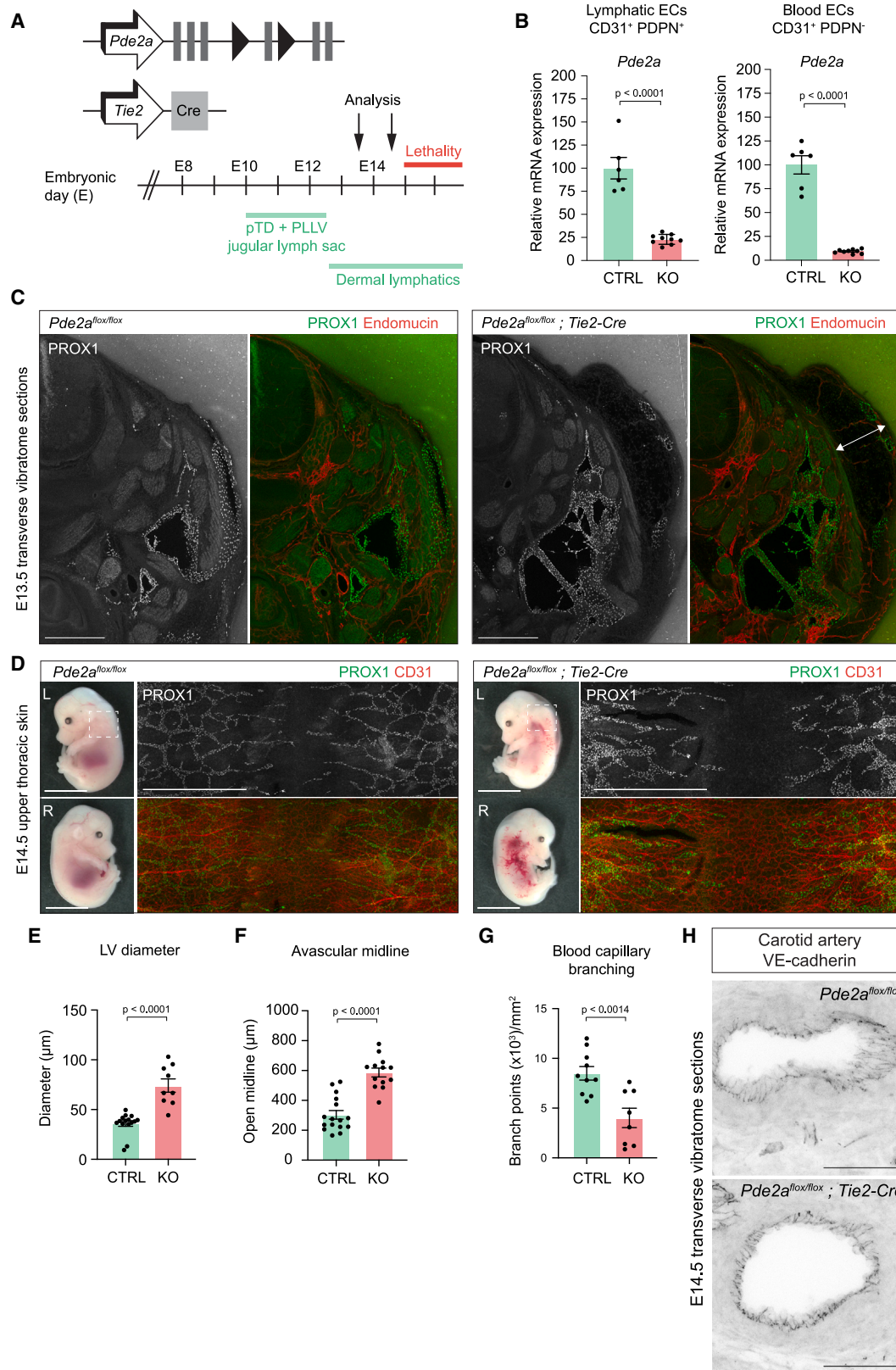
Global deletion of *Pde2a* (*Pde2a*$^{-/-}$) results in embryonic lethality around embryonic day (E)14.5–15.5, suggested to be caused by anemia, hemorrhages, and reduced fetal liver size.[25–27] In order to specifically investigate the role of PDE2A in LECs and BECs, we ablated *Pde2a* expression in BECs prior to LEC commitment using *Tie2-Cre* mice in combination with a newly generated floxed *Pde2a* allele (Figures 2A, S2A, and S2B). Efficient deletion of endothelial *Pde2a* was demonstrated by real-time PCR in E14.5-sorted CD31$^+$;podoplanin (PDPN)$^+$ LECs (77%) and CD31$^+$;PDPN$^-$ BECs (91%) (Figure 2B). Analysis of immunostained transverse vibratome sections of E13.5 and E14.5 embryos revealed massive enlargement of prospero homeobox 1 (PROX1)$^+$ lymph sacs in *Pde2a*$^{flox/flox}$; *Tie2-Cre* embryos compared with Cre-negative control embryos (Figures 2C, S3C, and S3D).

Furthermore, *Pde2a*$^{flox/flox}$; *Tie2-Cre* embryos exhibited large nuchal edema (Figure 2C) that can be indicative of a dysfunctional lymphatic vasculature.[28] *Pde2a*$^{flox/flox}$; *Tie2-Cre* embryos failed to form lympho-venous valves (LVVs), and mutant valve leaflets did not extend into the lumen of the cardinal vein (Figures S2E and S2F). Consistent with these findings, whole-mount immunostaining of E14.5 upper thoracic back skins revealed disturbed lymphangiogenesis with disconnected and enlarged LVs in *Pde2a*$^{flox/flox}$; *Tie2-Cre* embryos (Figures 2D–2F). A similar lymphatic phenotype was observed in neuropilin 2 (NRP2)$^+$ dermal LVs of global E14.5 *Pde2a*$^{-/-}$ mutant embryos but not littermate control embryos (Figure S2G).

Blood capillary branching was reduced in the midline region of *Pde2a*$^{flox/flox}$; *Tie2-Cre* embryos (Figure 2G), whereas VE-cadherin$^+$ E14.5 carotid artery diameter (Figure 2H) and overall large blood vessel morphology were normal (Endomucin$^+$ vessels in Figure 2C and CD31$^+$ larger vessels in Figure 2D).

Taken together, these results indicate that PDE2A plays an important role in lymphatic development.

In the absence of PDE2A expression, lymphatic junctions fail to mature *in vitro*

We next sought to analyze if loss of PDE2A could contribute to LV dysplasia through dysregulation of lymphatic junctions. HDLECs were cultured for 24, 48, 72, and 96 h on a 4 kPa substrate (Figure S3A) and plastic surfaces (Figure 3A) to correlate changes in protein levels with increasing lymphatic monolayer confluency and junctional maturation. As expected, protein expression of CLDN5, a major lymphatic junctional molecule,[18]

was induced with increasing monolayer confluency, demonstrating the formation of stable and mature lymphatic junctions (Figures 3A and S3B). Notably, VE-cadherin was highly expressed in immature lymphatic junctions, but expression levels were downregulated with increasing CLDN5 protein expression (Figure 3A).

Interestingly, PDE2A protein expression also increased with lymphatic monolayer maturation (Figures 3A and S3A). Immunofluorescence staining using antibodies against PDE2A and VE-cadherin further confirmed immunoblot data (Figures 3B and S3B). By contrast, PDE2A levels remained low and unaltered in HUVECs cultured for 24, 48, and 72 h, despite the expected strong increase in VE-cadherin and a moderate increase in CLDN5 protein signal (Figure 3A).

To assess the functional consequence of PDE2A loss, we performed siRNA-mediated knockdown of *PDE2A* expression in HDLECs with increasing monolayer confluency states. Interestingly, loss of PDE2A only resulted in decreased CLDN5 expression levels (Figures 3C green arrow and 3D) in stable lymphatic monolayers (72 h culture) having high PDE2A protein levels (Figure 3A). We have previously shown that CLDN5 is a major junctional "gatekeeper" in HDLECs versus HUVECs,[18] suggesting that once HDLEC junctions disintegrate, VE-cadherin levels are also reduced (Figure 3C). Together, these data indicate that *PDE2A*-deficient LECs are defective in forming mature and stable CLDN5$^+$ junctions *in vitro*.
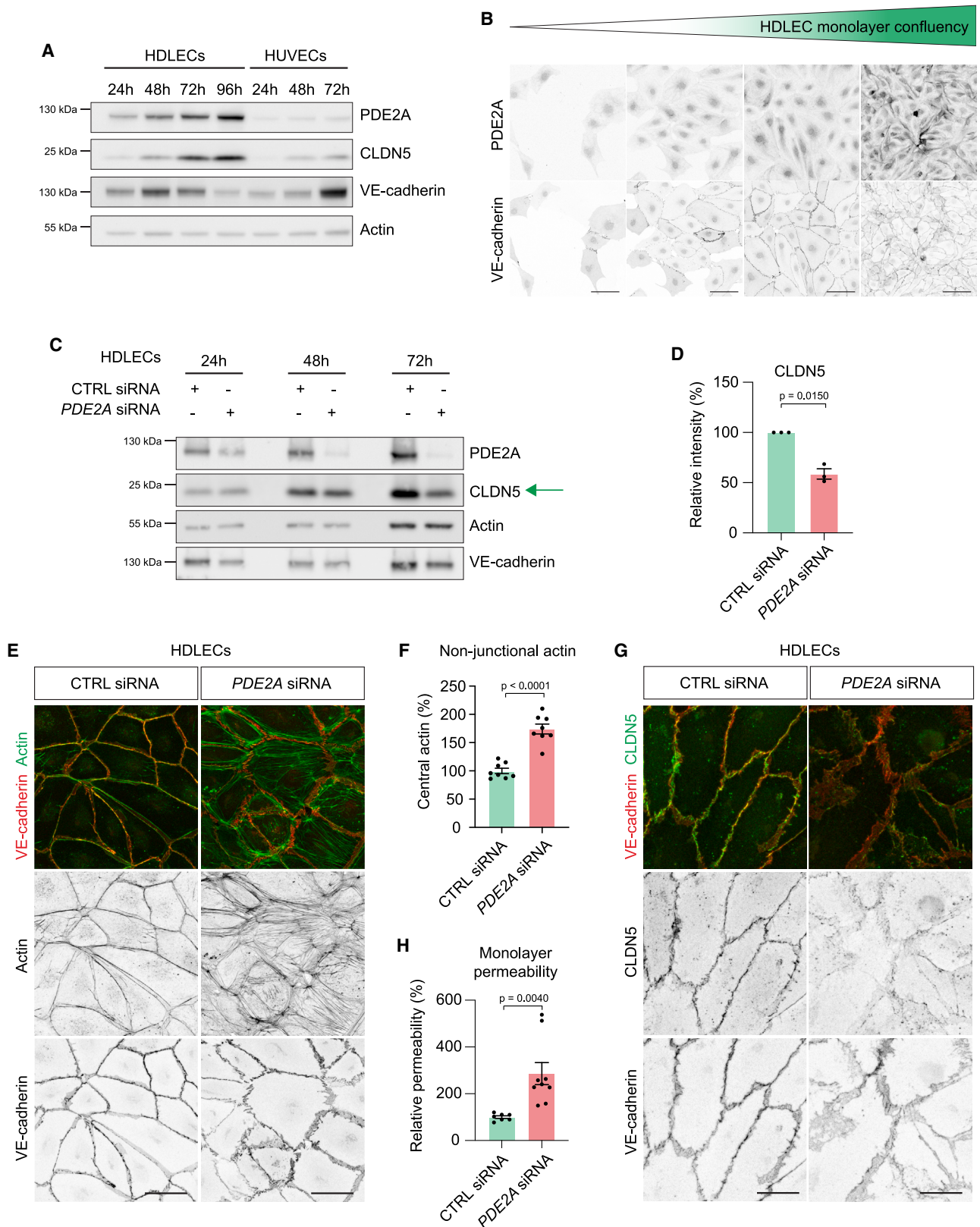
Upon siRNA-mediated knockdown of *PDE2A* expression, immunofluorescence analysis of VE-cadherin, actin, and CLDN5 further showed disruption of 72 h cultured HDLECs but not HUVECs (Figures S3C and S3D), characterized by decreased cortical actin (Figures 3E and 3F) and dispersed junctional CLDN5 (Figure 3G). Consistent with these morphological findings, deletion of *PDE2A* impaired barrier function and led to increased HDLEC, but not HUVEC, monolayer permeability (Figures 3H and S3E). Conclusively, in contrast to venous BECs, PDE2A expression is strongly upregulated in LECs during the formation of stable cell-cell junctions. Conversely, in the absence of PDE2A, lymphatic junctions fail to stabilize.

Loss of PDE2A expression prevents LEC contact inhibition and cell cycle arrest *in vitro*

A hallmark of EC junctional maturation is halted proliferation, contact inhibition, and cell cycle arrest. We therefore sought to investigate if PDE2A might play a role in controlling these

---

Figure 2. Endothelial *Pde2a* deletion in the *Tie2*-lineage impairs embryonic lymphatic development

(A) Scheme of the genetic constructs and analyzed embryonic stages (E).

(B) Relative mRNA expression of *Pde2a* in LECs and BECs sorted from E14.5 back skins of n = 6 *Pde2a*$^{flox/flox}$; *Tie2-Cre* embryos (KO) and n = 9 *Pde2a*$^{flox/flox}$ littermate embryos (CTRL). Mean ± SEM, p value: unpaired Student's t test.

(C) Representative immunofluorescence staining of 100 μm transverse vibratome sections from E13.5 KO and CTRL embryos stained with antibodies against PROX1 (green) and endomucin (red). Single channel images for PROX1 are shown. KO embryos display enlarged jugular lymphatic structures and nuchal edema (arrow). Scale bars, 500 μm.

(D) Representative brightfield images of E14.5 *Pde2a* KO and CTRL embryos and immunofluorescence staining of whole-mount upper thoracic back skins stained with antibodies against PROX1 (green) and CD31 (red). Single channel images for PROX1 are shown. Scale bars, 500 μm.

(E and F) Quantification of LV diameter (E) and avascular midline (F) in E14.5 upper thoracic back skins of n = 9–13 KO and n = 15–16 CTRL embryos. Mean ± SEM, p value: unpaired Student's t test.

(G) Quantification of blood capillary branching in E14.5 upper thoracic back skins of n = 8 KO and n = 10 CTRL embryos. Mean ± SEM, p value: unpaired Student's t test.

(H) Representative immunofluorescence staining of the carotid artery in 100 μm transverse vibratome sections of E14.5 KO and CTRL embryos stained with an antibody against VE-cadherin. Notably, carotid artery morphology and VE-cadherin$^+$ junctions were not altered in KO embryos. Scale bars, 50 μm.

A — HDLECs / HUVECs Western blot: PDE2A (130 kDa), CLDN5 (25 kDa), VE-cadherin (130 kDa), Actin (55 kDa) at 24h, 48h, 72h, 96h (HDLECs) and 24h, 48h, 72h (HUVECs).

B — HDLEC monolayer confluency; PDE2A and VE-cadherin immunostaining.

C — HDLECs at 24h, 48h, 72h with CTRL siRNA (+/−) and PDE2A siRNA (−/+); Western blot for PDE2A (130 kDa), CLDN5 (25 kDa), Actin (55 kDa), VE-cadherin (130 kDa).

D — CLDN5 Relative intensity (%); p = 0.0150; CTRL siRNA vs PDE2A siRNA.

E — HDLECs; CTRL siRNA and PDE2A siRNA; VE-cadherin (red) Actin (green); Actin; VE-cadherin.

F — Non-junctional actin; Central actin (%); p < 0.0001; CTRL siRNA vs PDE2A siRNA.

G — HDLECs; CTRL siRNA and PDE2A siRNA; VE-cadherin (red) CLDN5 (green); CLDN5; VE-cadherin.

H — Monolayer permeability; Relative permeability (%); p = 0.0040; CTRL siRNA vs PDE2A siRNA.

(legend on next page)

processes in LECs. Using an RNA-seq approach, we first identified differentially expressed genes that are potentially involved in junctional maturation and contact inhibition by comparing CTRL siRNA-treated HDLECs with "loose" CLDN5^{Low} junctions and CTRL siRNA-treated HDLECs with "tight" CLDN5^{High} junctions (Figure 4A). To identify PDE2A-regulated genes that are potentially involved in lymphatic junctional maturation, CTRL siRNA-treated HDLECs with tight CLDN5^{High} junctions were further compared with *PDE2A* siRNA-treated HDLECs with tight CLDN5^{High} junctions (Figure 4B). GO term analysis revealed the downregulation of various GO terms associated with cell cycle transition, cell division, and proliferation and the upregulation of GO terms associated with cell junction organization and growth arrest upon junction maturation (Figure 4A). By contrast, loss of PDE2A reversed junctional stabilization- and proliferation-associated GO terms (Figure 4B), demonstrating a shift of gene expression toward a loose junctional state.

CLDN5 and gap junction protein alpha 4 (*GJA4*, connexin 37) mRNA expression was downregulated in the absence of PDE2A, whereas various proliferation markers were upregulated (Figures 4C and S3F). Consistently, *PDE2A* siRNA treatment of HDLECs grown to high density maintained the cells in a KI67$^+$ proliferative state (Figures 4D and 4E). Similarly, 5-bromo-2′-deoxyuridine (BrdU) incorporation was maintained only in high density HDLEC monolayers upon *PDE2A* siRNA treatment (Figure S3G).

Loss of endothelial PDE2A expression prevents lymphatic maturation and contact inhibition at later stages during embryonic development

To avoid early embryonic lethality and analyze lymphatic maturation *in vivo*, we crossed *Pde2a^{flox}* mice with tamoxifen-inducible *Cdh5-CreER^{T2}* mice. Cre-mediated *Pde2a* deletion was induced from E10.5 for 4 consecutive days, and embryos were analyzed at E17.5 (Figures 4F and 4G). At that stage, non-venous-derived LECs had been incorporated into the vessels, lateral dermal lymphatics had reached the dorsal midline, valves were formed, and lymphatic proliferation was found to decrease in the maturing plexus. mRNA expression of the proliferation marker *Mki67* was increased (42%) in E17.5-sorted CD31$^+$;PDPN$^+$ LECs from in *Pde2a$^{flox/flox}$; Cdh5-CreER^{T2}* mutant embryos compared with Cre-negative control embryos, despite a suboptimal deletion of

Pde2a (48%) (Figure 4H). Consistent with this finding, PROX1 whole-mount immunostaining of E17.5 upper thoracic back skins demonstrated a reduced number of PROX1^{High} valve regions (Figures 4I and 4J), with increased LV diameter and increased PROX1$^+$ cell number in *Pde2a$^{flox/flox}$; Cdh5-CreER^{T2}* mutant embryos compared with Cre-negative control embryos (Figures 4I and 4K). *Pde2a$^{flox/flox}$; Cdh5-CreER^{T2}* embryos were smaller and showed edema in the neck region compared with Cre-negative control embryos (Figure 4I). By contrast, sprouting of LYVE1$^+$ filopodia and VEGFR3 expression in the sprouting front and the maturing plexus was not affected even when *Pde2a$^{flox/flox}$; Cdh5-CreER^{T2}* mutant embryos were analyzed at E16.5 before the dorsal midline has closed (Figure S4A). Similarly, VEGFR3 expression in whole-mount immunostaining of E14.5 upper thoracic back skins was unaltered in *Pde2a$^{flox/flox}$; Tie2-Cre* embryos (Figures S4B and S4C), and *PDE2A* siRNA treatment of HDLECs did not result in changes of VEGFR3 mRNA and protein expression or VEGFR3 activation (Figures 4C, S4D, and S4E).

Taken together, in the absence of PDE2A, LECs fail to induce contact inhibition and downregulation of proliferation *in vitro* and in maturing areas of the embryonic dermal lymphatic network, whereas sprouting of dermal lymphatics was not affected by PDE2A.
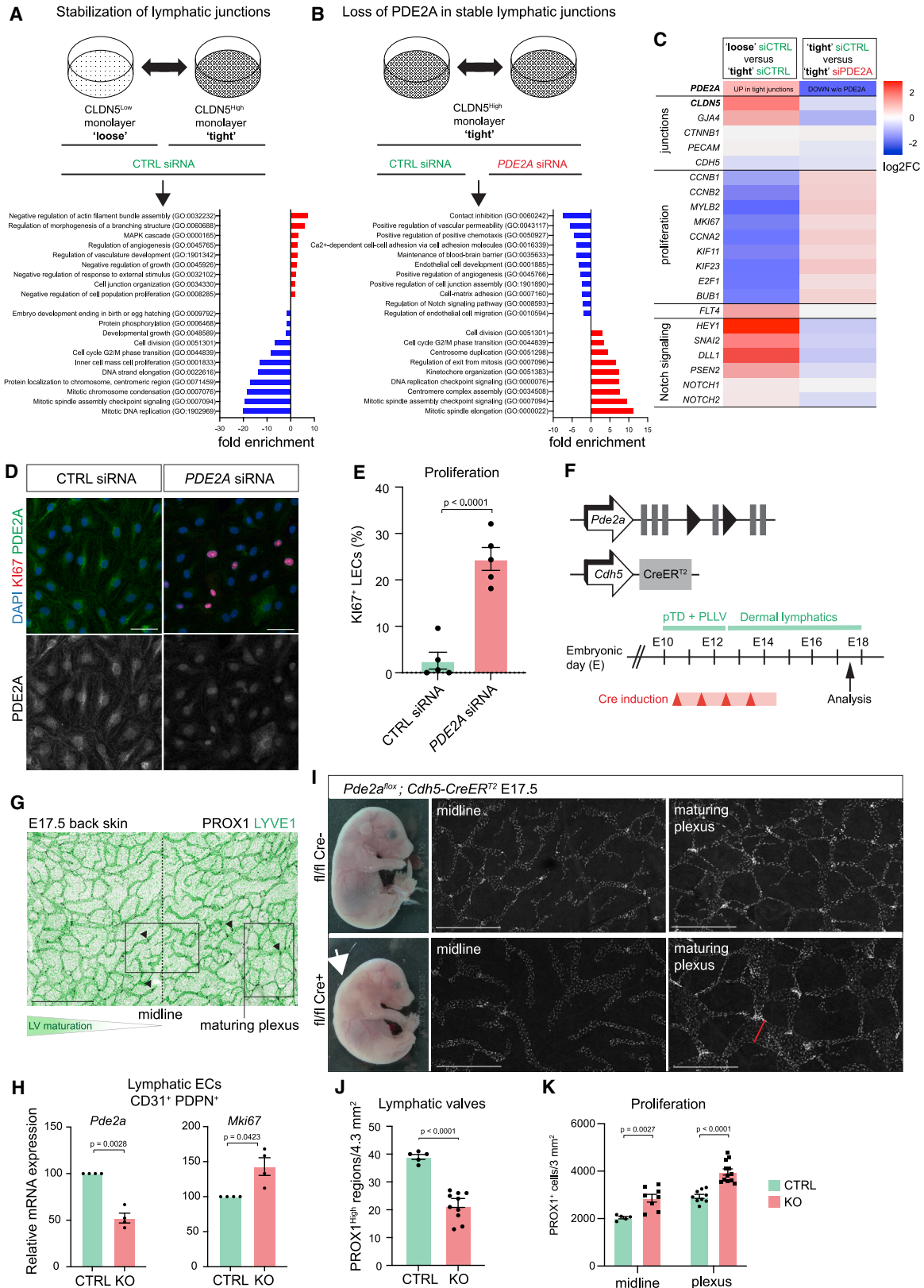
Loss of PDE2A selectively increases lymphatic cGMP levels in a cAMP-independent manner

Most studies on cAMP function in BECs have shown that increasing exogenous and endogenous cAMP levels stabilize BEC junctions,[29–31] whereas others have reported that prolonged elevation of cAMP destabilizes EC junctions and increases endothelial permeability.[32] Consistent with previous data in BECs,[33,34] we showed that incubation of LECs with cAMP derivatives stabilizes LEC barrier function (Figure S5A).

PDE2A regulates cellular cyclic monophosphate metabolism by catalyzing the hydrolysis of cAMP to AMP and cGMP to GMP, respectively.[35,36] Loss of PDE2A-mediated catalytic activity is therefore expected to increase lymphatic cAMP and/or cGMP levels that in turn could cause lymphatic dysfunction. We therefore sought to analyze if PDE2A differentially regulates cAMP and cGMP levels in HUVECs versus HDLECs. Loss of PDE2A function in HUVECs resulted in increased cAMP levels

---

Figure 3. Lymphatic junctions fail to mature in the absence of PDE2A

(A) Western blot analysis of HDLECs and HUVECs cultured on plastic substrate from 24 to 96 h and 72 h, respectively. Lysates were probed with antibodies against PDE2A, CLDN5, VE-cadherin, and actin as loading control.

(B) Representative immunofluorescence staining of HDLECs cultured on glass substrate from 24 to 96 h and stained with antibodies against PDE2A and VE-cadherin. With increasing monolayer confluency, PDE2A expression is increased. Scale bars, 50 μm.

(C) Western blot analysis of CTRL and *PDE2A* siRNA-treated HDLECs cultured for 24, 48, and 72 h. Lysates were probed with antibodies against PDE2A, CLDN5, VE-cadherin, and actin as loading control. Notably, in the absence of PDE2A, HDLECs fail to form CLDN5^{High} junctions (green arrow).

(D) Quantification of CLDN5 protein expression in 72 h CTRL and *PDE2A* siRNA-treated HDLECs from n = 3 independent experiments. Mean ± SEM, p value: one-sample t test.

(E) Representative immunofluorescence staining of 72 h CTRL and *PDE2A* siRNA-treated HDLECs stained with an antibody against VE-cadherin (red) and phalloidin (green, to visualize actin). Single channel images of VE-cadherin and phalloidin are shown. Scale bars, 50 μm.

(F) Quantification of relative central actin (total actin—junctional actin) from 72 h CTRL and *PDE2A* siRNA-treated HDLECs from n = 2 independent experiments. Mean ± SEM, p value: unpaired Student's t test.

(G) Representative immunofluorescence staining of 72 h CTRL and *PDE2A* siRNA-treated HDLECs using antibodies against VE-cadherin (red) and CLDN5 (green). Single channel images are shown. Scale bars, 20 μm.

(H) Quantification of monolayer permeability to 40 kDa FITC-dextran in CTRL and *PDE2A* siRNA-treated HDLECs from n = 2 independent experiments, mean ± SEM, p value: unpaired Student's t test.

A Stabilization of lymphatic junctions

B Loss of PDE2A in stable lymphatic junctions

C

D CTRL siRNA / PDE2A siRNA
DAPI KI67 PDE2A
PDE2A

E Proliferation

F

G E17.5 back skin — PROX1 LYVE1
LV maturation / midline / maturing plexus

I *Pde2a^flox ; Cdh5-CreER^T2* E17.5
fl/fl Cre- : midline / maturing plexus
fl/fl Cre+ : midline / maturing plexus

H Lymphatic ECs CD31+ PDPN+
Pde2a — p = 0.0028
Mki67 — p = 0.0423

J Lymphatic valves — p < 0.0001

K Proliferation
midline p = 0.0027, plexus p < 0.0001
CTRL / KO

(legend on next page)

(Figure 5A).[22] By contrast, in HDLECs, cAMP levels were not significantly altered upon *PDE2A* knockdown (Figure 5A). These findings suggested that PDE2A likely regulates lymphatic maturation via the modulation of cGMP levels instead. In agreement with this, siRNA-mediated deletion of *PDE2A* elevated cGMP levels in HDLECs compared with control HDLECs (Figure 5A).

In parallel, we used live-cell imaging and a plasma membrane targeted biosensor pmEpac1-camps (Figure 5B) to measure local cAMP responses at the membrane of HDLECs as previously described for HUVECs.[22] First, we compared cAMP responses with the beta-adrenergic agonist isoprenaline (ISO, 1 μM) with and without PDE2 (BAY60-7550, 100 nM) or PDE3 inhibition (cilostamide, 10 μM). Both inhibitors had no effect on ISO-induced production of cAMP, compared with ISO alone (Figure 5B). Next, we assessed the effects of PDE2 and PDE3 inhibition on atrial natriuretic peptide (ANP)-induced cAMP responses measured as cGMP/cAMP crosstalk by the pmEpac1-camps biosensor (Figure 5C). When HDLECs were stimulated with ANP alone, a negligible increase in cAMP levels was detected. This was likely due to high PDE2A activity in HDLECs, where ANP-generated cGMP can enhance PDE2A-mediated cAMP degradation and thus only modestly increases cAMP levels as a result of this negative cGMP/cAMP crosstalk. In support of this hypothesis, inhibition of PDE2A, but not of PDE3A, could unmask the stimulatory effect of ANP on cAMP levels in HDLECs, in contrast to HUVECs, where PDE3A has been identified as the main regulator of membrane cGMP/cAMP crosstalk, whereas PDE2 expression and contribution were negligible.[22] Our measurements in HDLECs showed that PDE2, but not PDE3, inhibition significantly augmented ANP/cGMP responses (Figures 5C and 5D).

Interestingly, PDE2A inhibition by BAY60-7550 abolished all cGMP-hydrolyzing capacity of LECs at 24 and 96 h of culture (Figure 5E), demonstrating that under physiological conditions, PDE2A plays a central role in the control of cGMP second messenger signaling in LECs. Furthermore, we found that other PDEs, namely PDE12, PDE10A, PDE4B, PDE4D, PDE6D, and PDE8A, were not altered upon siRNA-mediated knockdown of

PDE2A (Figure S5B), suggesting that they are unlikely to compensate for the loss of PDE2A in LECs.

To study if an increase of cGMP in LECs would show junctional disruption similar to the loss of PDE2A, we incubated mature HDLEC monolayers with 250 μM 8-Br-cGMP for 48 h. As expected, immunofluorescence analysis of VE-cadherin and actin showed disruption of stable HDLEC monolayers with loss of cortical actin upon treatment with 8-Br-cGMP (Figures 5F and 5G).
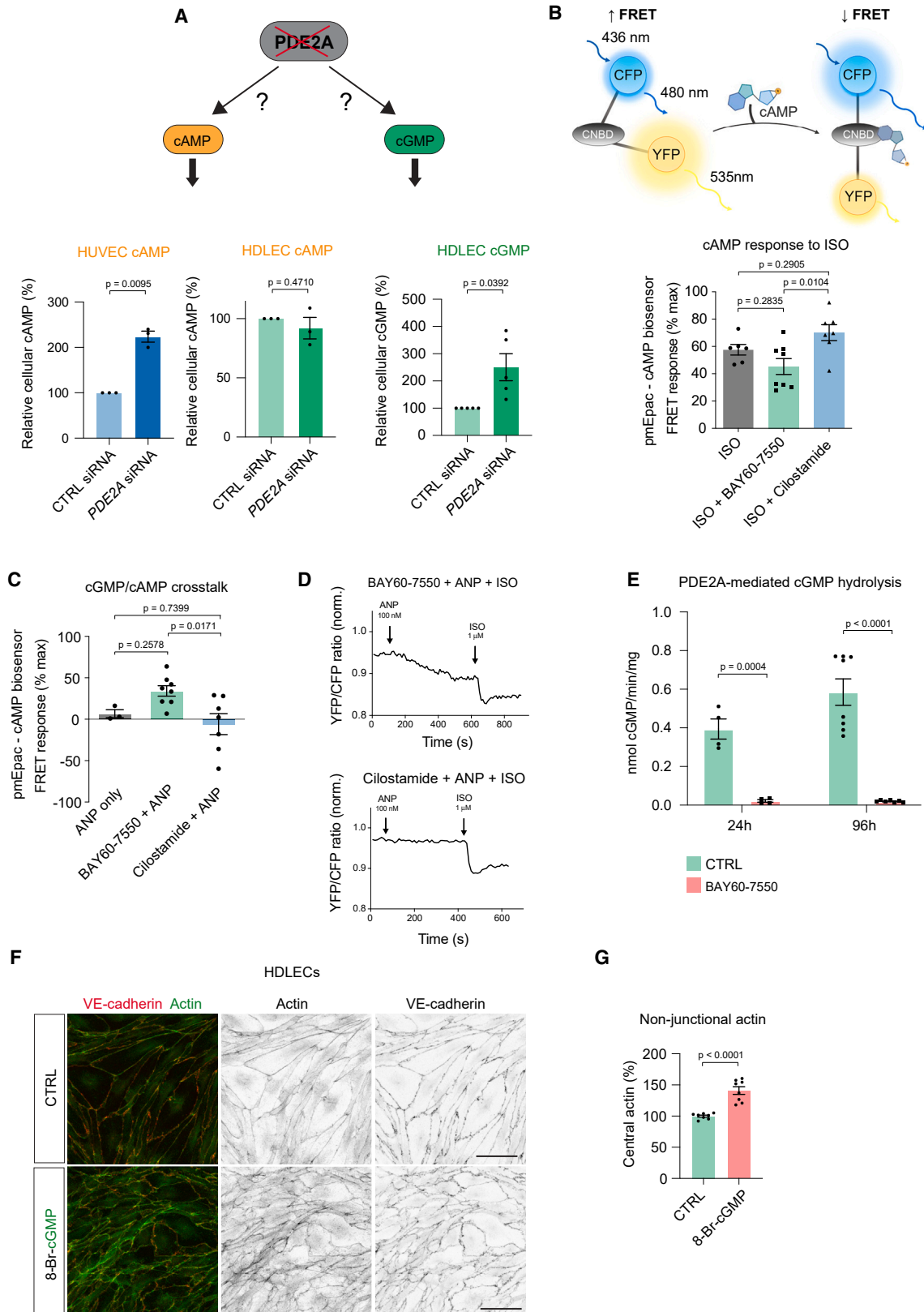
Conclusively, loss of PDE2A selectively increases lymphatic cGMP but not cAMP levels. Increased LEC cGMP levels result in junctional disruption and a decrease in cortical actin similar to what has been observed upon *PDE2A* deletion.

PDE2A modulates a crosstalk between cGMP, p38, and NOTCH signaling in LECs

Finally, we sought to analyze how elevated cGMP levels lead to junctional disruption and increased proliferation. cGMP has been shown to activate p38 mitogen-activated protein kinase (p38).[37,38] Consistently, in *PDE2A*-deficient HDLECs, increased cGMP levels induced p38 phosphorylation (Figures 6A and 6B), suggesting p38 signaling to regulate signaling downstream of PDE2A in LECs. In agreement with this finding, incubation of *PDE2A*-deficient HDLECs with the p38 inhibitor SB203580 prevented aberrant proliferation (Figures 6C and S5C). Inhibition of p38 has been previously described to upregulate NOTCH target gene expression.[39] Notably, GO term analysis and quantitative real-time PCR highlighted that NOTCH signaling (GO:0008593) was downregulated upon the deletion of *PDE2A* in stable lymphatic junctions (Figures 4B and S3F). Furthermore, we have previously shown that siRNA-mediated knockdown of *NOTCH1* and NOTCH inhibition via N-[N-(3,5-difluorophenacetyl-L-alanyl)]-(S)-phenylglycine t-butyl ester (DAPT) resulted in increased proliferation,[40] suggesting that loss of PDE2A increased cGMP, and p38 activation could regulate lymphatic junctions by interference with NOTCH activation and consecutively NOTCH-induced cell cycle arrest.

Figure 4. Loss of PDE2A prevents lymphatic contact inhibition and maturation *in vitro* and *in vivo*

(A) Global transcriptome analysis comparing HDLECs grown on physiological 4 kPa stiffness substrates with loose CLDN5[Low] junctions and tight CLDN5[High] junctions (n = 2 biological replicates) and enrichment of selected GO terms. Upregulated and downregulated GO terms are represented in red and blue, respectively.

(B) Global transcriptome analysis of CTRL and *PDE2A* siRNA-treated HDLECs with tight CLDN5[High] junctions (n = 2 biological replicates) and enrichment of selected GO terms. Upregulated and downregulated GO terms are represented in red and blue, respectively.

(C) Selected upregulated and downregulated transcripts regulated by PDE2A are shown.

(D) Representative immunofluorescence staining of 72 h CTRL and *PDE2A* siRNA-treated HDLECs stained with antibodies against KI67 (magenta), PDE2A (green), and DAPI (blue). Single channel images for PDE2A are shown. Scale bars, 50 μm.

(E) Quantification of the percentage of KI67^{+} HDLECs treated with CTRL and *PDE2A* siRNA (n = 5 independent experiments). Mean ± SEM, p value: unpaired Student's t test.

(F) Scheme of the genetic constructs and analyzed embryonic stages. Time points for 4-hydroxytamoxifen injections (Cre induction) are indicated.

(G) Representative whole-mount immunofluorescence staining of a wild-type E17.5 upper thoracic back skin stained with antibodies against PROX1 (gray) and LYVE1 (green) showing the midline region and the maturing lymphatic plexus region analyzed in (C).

(H) Relative mRNA expression of *Pde2a* and *Mki67* in LECs sorted from E17.5 back skins of n = 4 *Pde2a^{flox/flox}; Cdh5-CreER^{T2}* embryos (knockout [KO]) and n = 4 *Pde2a^{flox/flox}* littermate embryos (CTRL). Mean ± SEM, p value: one-sample t test.

(I) Whole-mount immunofluorescence staining of E17.5 upper thoracic back skin midline and maturing plexus from *Pde2a^{flox/flox}; Cdh5-CreER^{T2}* (KO) and *Pde2a^{flox/flox}* (CTRL) embryos stained with an antibody against PROX1. Scale bars, 500 μm. Representative images of *Pde2a^{flox/flox}; Cdh5-CreER^{T2}* knockout and *Pde2a^{flox/flox}* control embryos. White arrow shows edema in the neck region.

(J) Quantification of lymphatic valves (as PROX1[High] regions) in the E17.5 upper thoracic back skin of n = 5 KO and n = 3 CTRL embryos. Mean ± SEM, p value: unpaired Student's t test.

(K) Quantification of PROX1^{+} cells in midline and maturing plexus of n = 5 KO and n = 3 CTRL embryos. Mean ± SEM, p value: unpaired Student's t test.

A

HUVEC cAMP

HDLEC cAMP

HDLEC cGMP

B

cAMP response to ISO

C cGMP/cAMP crosstalk

D BAY60-7550 + ANP + ISO

Cilostamide + ANP + ISO

E PDE2A-mediated cGMP hydrolysis

CTRL
BAY60-7550

F HDLECs

VE-cadherin Actin | Actin | VE-cadherin

CTRL

8-Br-cGMP

G

Non-junctional actin

(legend on next page)

In agreement with a potential PDE2A/p38/NOTCH-signaling axis, we found that mRNA expression of the Notch target gene *Hey1* was decreased in sorted CD31$^+$; PDPN$^+$ LECs from *Pde2a$^{flox/flox}$; Tie2-Cre* mutant embryos in comparison to *Pde2a$^{flox/flox}$* control embryos (Figure S5D). Blocking all canonical NOTCH activity using DAPT resulted not only in the loss of nuclear NOTCH1 intracellular domain (NICD) as expected but also in the dispersion of junctional molecules VE-cadherin and CLDN5 (Figures S5E and S5F). To demonstrate a functional link between PDE2A and NOTCH signaling in LECs, we analyzed NOTCH signaling in HDLECs upon soluble DLL4 (sDLL4) stimulation in the presence or absence (siRNA-mediated knockdown) of *PDE2A* (Figures 6D–6G). sDLL4-mediated activation of NOTCH restored nuclear NICD (Figures 6D and 6E) and was sufficient to rescue high CLDN5 expression in *PDE2A*-deleted HDLECs, suggesting mature lymphatic junctions and intact cell cycle arrest (Figures S5G and S5H). Indeed, immunofluorescence analysis of VE-cadherin and CLDN5 showed normal junctional architecture in *PDE2A*-deleted HDLECs upon sDLL4-mediated NOTCH activation (Figures 6F and 6G). Ultimately, treatment of *PDE2A*-deleted HDLECs with the p38 inhibitor SB203580 restored nuclear NICD (Figures 6H and 6I), demonstrating that p38 signaling regulates NOTCH-mediated contact inhibition downstream of PDE2A-regulated cGMP levels.

Deletion of *Pde2a* in postnatal mesenteric LVs results in abnormal formation of lymphatic valves

To understand if PDE2A also plays a role in postnatal LVs, we analyzed PDE2A expression in LVs using whole-mount immunostaining of postnatal day (P)11 mesenteries (Figure 7A). Notably, PDE2A expression was strongly enriched in the lower valve sinus selectively in valves of the collecting and large pre-collecting LVs (Figure 7B), but not in smaller caliber vessels. Therefore, we studied the postnatal function of PDE2A with a focus on large lymphatic valves and crossed *Pde2a^{flox}* mice with tamoxifen-inducible *Prox1-CreER^{T2}* mice. Cre-mediated *Pde2a* deletion was induced from P2 and P3 and analyzed at P11 (Figure 7C). Although LV diameter and smooth muscle cell coverage were not altered at P11 (Figures 7D, S6A, and S6B), loss of PDE2A re-sulted in abnormal morphology and reduced numbers of large valves in *Pde2a$^{flox/flox}$; Prox1-CreER^{T2}* mutant mice compared with Cre-negative control mice (Figures 7F and 7G). In agreement with this, CLDN5$^+$ junctions of the collecting lymphatic valve sinus appeared more jagged and discontinuous (Figure 7G).

These findings suggest that tight regulation of LEC junctions through PDE2A-mediated control of cGMP might be particularly important to maintain proper function of the large valves in postnatal LVs.

Taken together, our study uncovers a mechanism by which PDE2A regulates lymphatic junctional maturation through cGMP-mediated control of Notch signaling during embryonic development (Figure S7). During postnatal development of mesenteric LVs, PDE2A continues to play an important role by regulating the formation of lymphatic valves (Figure S7).

DISCUSSION

Selective barrier control can be achieved through exclusive expression of junction-controlling molecules in different EC types.[42,43] However, other molecules, such as VE-cadherin[16,17] and EphB4,[18,19] have been shown to have multifaceted roles in junctional regulation across different vascular beds, despite similar expression patterns. Although most studies show that increased cAMP levels strengthen junctional stability in LECs and BECs,[29-31] the role of cGMP in junctional integrity remains poorly understood. Similar to PDE2 inhibition,[44] we show that knockdown of PDE2A in HUVECs led to increased cAMP levels, suggesting that in the absence of PDE2A, BECs might show altered junctions. However, although blood capillary branching was slightly decreased in embryonic back skin upon endothelial *Pde2a* deletion at E14.5, we did not find morphological evidence that BEC junctions or vessel architecture were altered, suggesting that alterations of cAMP levels in BECs might be normalized through other PDEs or endogenous cAMP accumulation is not sufficient to induce BEC dysfunction at this developmental stage. Intriguingly, we found that loss of junctional maturation in PDE2A-deficient LECs is caused by the accumulation of

---

Figure 5. Loss of PDE2A increases lymphatic cGMP levels

(A) (Left) Quantification of relative cAMP levels in CTRL and *PDE2A* siRNA-treated HDLECs and HUVECs from n = 3 independent experiments per cell type. Mean ± SEM, p value: one-sample t test. (Right) Quantification of relative cGMP levels in CTRL and *PDE2A* siRNA-treated HDLECs from n = 5 independent experiments. Mean ± SEM, p value: one-sample t test.

(B) Scheme of the Förster resonance energy transfer (FRET) Epac1-camps biosensor. cAMP binding leads to a conformational change and increased spatial separation between both fluorescent probes, resulting in a decrease in the FRET signal. Quantification of FRET response in HDLECs transduced with the plasma membrane targeted biosensor, pmEpac1-camps, upon treatment with isoprenaline (ISO, beta-adrenergic agonist), ISO + BAY60-7550 (PDE2 inhibitor), or ISO + cilostamide (PDE3 inhibitor). Single points represent single cells from n = 3 independent experiments. Mean ± SEM, p value: one-way ANOVA with Turkey's multiple comparison test.

(C) Quantification of FRET change in HDLECs transduced with pmEpac1-camps and treated with atrial natriuretic peptide (ANP), BAY60-7550 + ANP, or cilostamide + ANP. Notably, PDE2 inhibition, but not PDE3 inhibition, significantly increases ANP/cAMP response. Single points represent single cells from n = 3 independent experiments. Mean ± SEM, p value: one-way ANOVA with Turkey's multiple comparison test.

(D) Representative FRET traces show responses to treatment with BAY60-7550 + ANP + ISO or cilostamide + ANP + ISO in pmEpac1-camps-transduced HDLECs. A decrease in yellow fluorescent protein (YFP)/cyan fluorescent protein (CFP) ratio corresponds to an increase in intracellular cAMP levels.

(E) PDE2 activity measured as a rate of cGMP hydrolysis in HDLECs culture for 24 or 96 h. Measurements were performed with CTRL or PDE2A inhibition (BAY60-7550). n = 2 independent experiments after 24 h, n = 4 independent experiments after 96 h. Mean ± SEM, p value: unpaired Student's t test with Welch's correction.

(F) Representative immunofluorescence staining of CTRL and 8-Br-cGMP-treated HDLECs stained with an antibody against VE-cadherin (red) and phalloidin (green, to visualize actin). Single channel images are shown. Scale bars, 50 μm.

(G) Quantification of relative central actin (total actin—junctional actin) from CTRL and 8-Br-cGMP-treated HDLECs from n = 3 independent experiments. Mean ± SEM, p value: unpaired Student's t test.
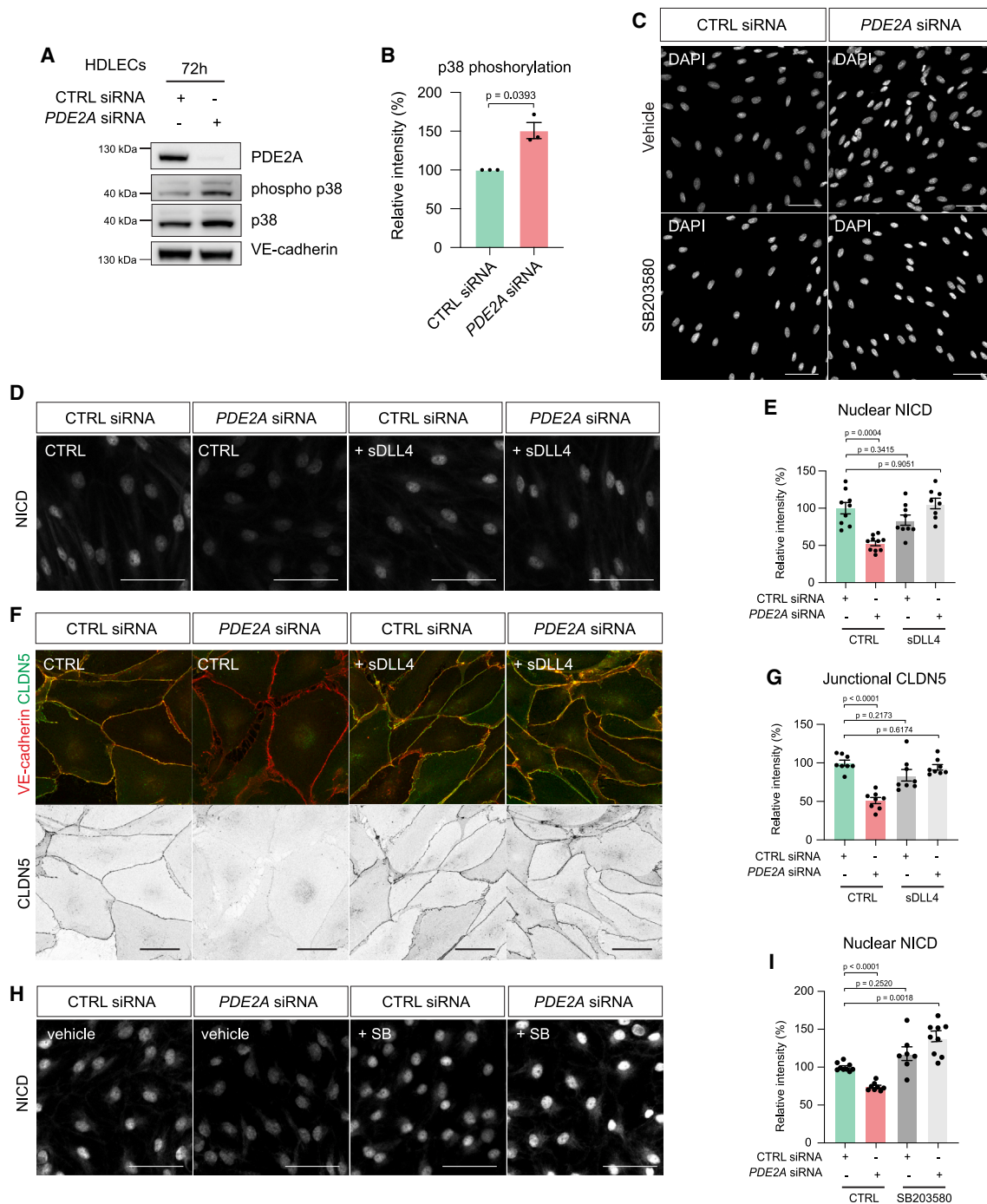
Figure 6. P38 inhibition and NOTCH signaling activation restores lymphatic junctional maturation

(A) Western blot analysis of CTRL and *PDE2A* siRNA-treated HDLECs cultured for 72 h. Lysates were probed with antibodies against PDE2A, phospho-p38, p38, and VE-cadherin as loading control.

(B) Quantification of p38 phosphorylation in CTRL and *PDE2A* siRNA-treated HDLECs from n = 3 independent experiments. Mean ± SEM, p value: one-sample t test.

(C) DAPI-stained HDLECs (as a measure of proliferation) treated with CTRL and *PDE2A* siRNA and vehicle or the p38 inhibitor SB203580, quantification is shown in Figure S5C.

(D) Immunofluorescence staining of CTRL and *PDE2A* siRNA-treated HDLECs incubated for 24 h with or without soluble DLL4 (sDLL4) using an antibody against NICD.

(E) Quantification of nuclear NICD from n = 2 independent experiments. Mean ± SEM, p value: one-way ANOVA with Dunnett's T3 multiple comparisons test.

(F) Representative immunofluorescence staining of CTRL and *PDE2A* siRNA-treated HDLECs incubated for 24 h with or without soluble DLL4 (sDLL4) using antibodies against CLDN5 (green) and VE-cadherin (red). Single channel images are shown for CLDN5.

(legend continued on next page)

intracellular cGMP but not cAMP. By contrast, compensation of dysregulated lymphatic cGMP levels is not likely to occur because we show for that PDE2A is the only enzyme to hydrolyze cGMP in LECs.

In agreement with our data, inhibition of PDE3A, using cilostamide, did not alter LV permeability when albumin flux across the collecting lymphatic wall was measured in isolated LVs from adult wild-type mice.[45] However, inhibition of PDE3 restored mesenteric collecting LV integrity in diabetic mice[45] and improved LV count and flow in a lymphedema mouse model.[46] The specific cellular populations responsible for these PDE2A and PDE3A-mediated effects remain to be investigated.

LVVs were impaired in E14.5 $Pde2a^{flox/flox}$; $Tie2$-Cre embryos. Notably, retrograde flow from the cardinal vein due to dysfunctional LVVs has been previously shown to contribute to the formation of blood-filled lymphatics and reduced lymphatic valves.[47] However, we did not observe blood-filled lymphatics in $Pde2a^{flox/flox}$; $Cdh5$-$CreER^{T2}$ embryos, demonstrating that the observed lymphatic phenotypes are LEC-autonomous.

At E14.5, global $Pde2a^{-/-}$ and $Pde2a^{flox/flox}$; $Tie2$-Cre embryos exhibited similar lymphatic and non-lymphatic phenotypes such as reduced size of the fetal liver and embryonic death at E14.5–15.5.[25,26] It is unlikely that loss of lymphatic PDE2A causes embryonic death in $Pde2a^{flox/flox}$; $Tie2$-Cre embryos. Therefore, our findings rather suggest that the loss of $Pde2a$ in other cell types of the Tie2^{+} lineage is causing embryonic defects and lethality. Future studies will delineate the contribution of different cell types of the Tie2^{+} lineage.

NOTCH has been shown to regulate general lymphatic growth, sprouting, proliferation, and valve morphogenesis.[40,48–51] Here, we identified a pleiotropic role of NOTCH signaling in LEC contact inhibition, which is modulated through crosstalk with PDE2A-regulated cGMP signaling. It needs to be further explored if this lymphatic-specific crosstalk might be regulated via changes in NOTCH signaling strength.[52]

An intimate relationship between PDE2A and NOTCH signaling is further supported by the finding that the NOTCH-targeting miRNA miR-139-$5p$[53] is located within the second intron of the $PDE2A/Pde2a$ host gene.[54] miR-139-$5p$ has been shown to correlate with $PDE2A$ expression, suggesting a potential inhibitory function on this gene.[54] Although we did not expect the second intron of the $Pde2a$ host gene to be dysregulated, given that Cre-induced recombination targets exon 4, we analyzed the expression of miR-139-$5p$ in isolated lung ECs from 8-week-old control and mutant $Pde2a^{flox}$; $Cdh5$-$CreER^{T2}$ mice. miR-139-$5p$ expression was not altered in $Pde2a$-mutant ECs (Figures S6C and S6D). Additionally, we investigated miR-139-$5p$ expression upon siRNA-mediated $PDE2A$ deletion in HDLECs to exclude negative feedback on miR-139-$5p$ expression. As expected, miR-139-$5p$ expression was not altered in CTRL versus $PDE2A$ siRNA-treated HDLECs (Figure S6E).

The pleiotropic p38 signaling cascade has been shown to be induced in ECs through different cellular stresses,[55,56] and p38 induces blood endothelial barrier dysfunction.[57] cGMP has been previously shown to activate p38.[37,38] Consistently, we also found that loss of PDE2A and elevated cGMP levels activate p38 in LECs. In turn, inhibition of p38 in $PDE2A$-deficient LECs rescued aberrant proliferation and nuclear NICD. Although NOTCH and p38 have pleiotropic functions and are therefore improbable therapeutic targets to specifically modulate lymphatic junctional integrity, targeting PDE2A could present a realistic opportunity.

In postnatal mesenteric LVs, PDE2A was enriched specifically in the sinus bottom of collecting lymphatic valves. Deletion of lymphatic PDE2A at P2/3 resulted in an abnormal shape of collecting lymphatic valves at P11, suggesting that PDE2A might have a more prominent role in areas that are exposed to high mechanical strain. In agreement with this, CLDN5^{+} junctions in the sinus of Pde2a-deleted valves appeared more jagged and discontinuous. We have previously shown that loss of CLDN5 in P11 mesenteries does not result in LEC junction breakdown in P11 mesenteries,[18] supporting our model that PDE2A regulates a contact inhibition signaling cascade rather than directly modulating a selected junctional adhesion molecule. Although the lymphatic valves are the first anatomical vessel structures that are impacted by the loss of PDE2A, it is likely that the lymphatic junctions of collecting LVs might be dysfunctional at a later stage. Recently, proliferating valve sinus LECs were elegantly shown to provide the main source for maintenance and repair of lymphatic valves in adult mice.[58] Future studies should analyze if PDE2A[High] valves sinus LECs will later give rise to this LEC population. To our knowledge, PDE2A is the first known molecule to distinguish between the valves of different mesenteric LVs during postnatal development.

We did not analyze button junctions during embryonic development because the proportion of button junctions is only 6% at E 17.5 and increases only after birth.[59] At P11, we did not yet observe mature button junctions in the mesenteries of CTRL $Pde2a^{flox/flox}$ mice. In line with our findings that PDE2A controls tight junctions, a state that applies to zippered junctions, we hypothesize that PDE2A has a more important role in LECs of collecting and larger pre-collecting vessels. However, future studies should investigate the loss of PDE2A in the zipper and button junctions of adult mice.
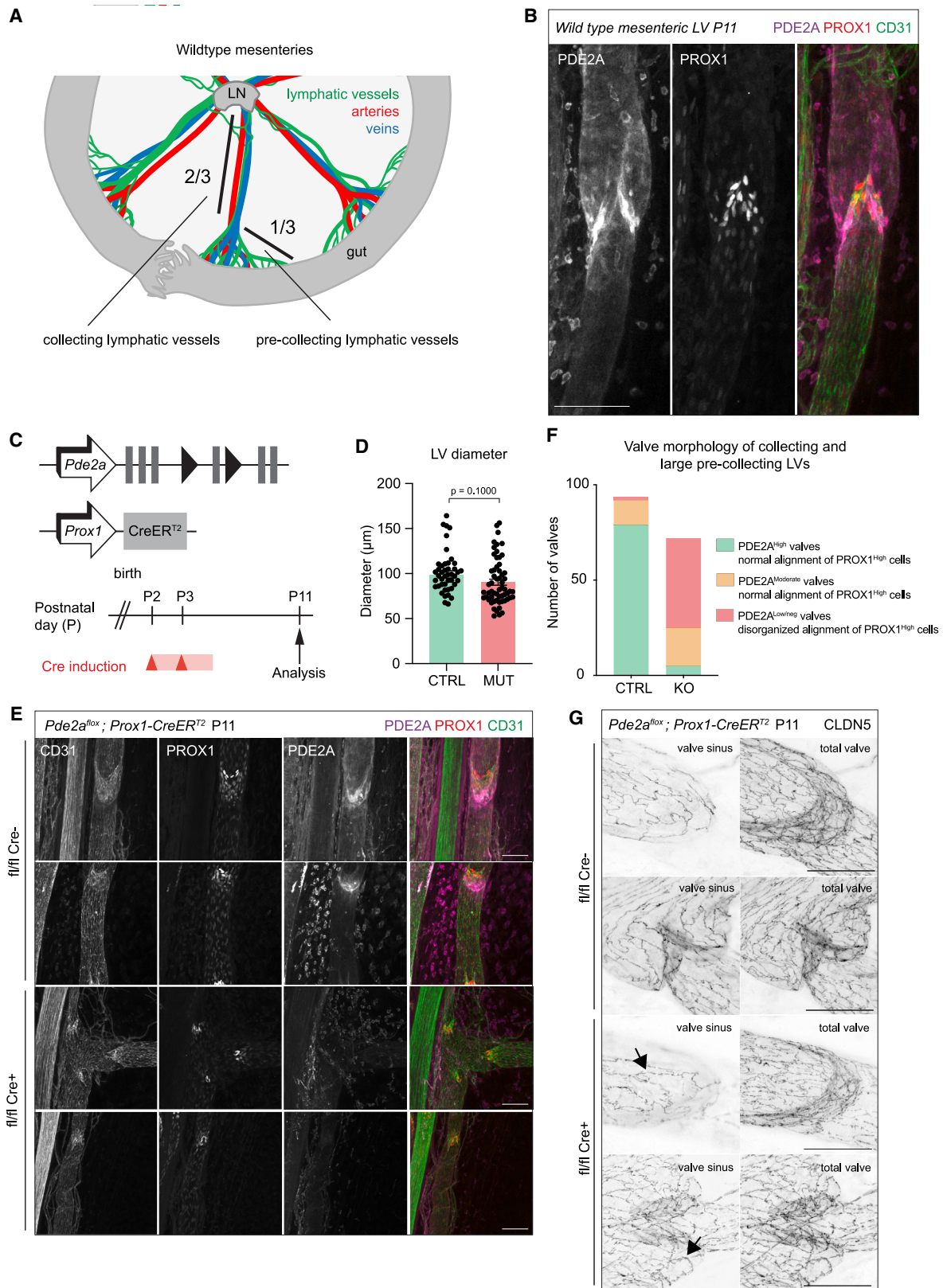
Although our assessment of lymphatic PDE2A function was limited to embryonic and postnatal developmental stages, the identified mechanism may be targetable to control lymphatic leakage or regrowth. Altered lymphatic junctional integrity has been implicated in a variety of pathological conditions, highlighting the need to understand the underlying mechanisms. For example, collecting vessel permeability is increased upon infection with $Yersinia$ $pseudotuberculosis$,[60] which results in the development of fibrotic processes,[61] increased inflammation, and compromised immunity due to reduced flow of lymph and immune cell transport to the lymph nodes (LNs).[62] Excessive leakage of lymph, caused by dysfunctional lymphatic endothelial

(G) Quantification of CLDN5 protein in VE-cadherin[+] junctions from n = 2 independent experiments. Mean ± SEM, p value: one-way ANOVA with Dunnett's T3 multiple comparisons test.

(H) Representative immunofluorescence staining of CTRL and $PDE2A$ siRNA-treated HDLECs incubated for 24 h with vehicle or the p38 inhibitor SB203580 (SB) using an antibody against NICD.

(I) Quantification of nuclear NICD from n = 2 independent experiments. Mean ± SEM, p value: one-way ANOVA with Dunnett's T3 multiple comparisons test.

A Wildtype mesenteries

lymphatic vessels (green)
arteries (red)
veins (blue)

LN
2/3
1/3
gut

collecting lymphatic vessels
pre-collecting lymphatic vessels

B *Wild type mesenteric LV P11*   PDE2A PROX1 CD31

PDE2A   PROX1

C
Pde2a
Prox1 CreER^T2

birth
Postnatal day (P)   P2 P3   P11

Cre induction
Analysis

D LV diameter

p = 0.1000

Diameter (µm)
200
150
100
50
0
CTRL   MUT

F Valve morphology of collecting and large pre-collecting LVs

Number of valves
100
50
0
CTRL   KO

PDE2A^High valves
normal alignment of PROX1^High cells

PDE2A^Moderate valves
normal alignment of PROX1^High cells

PDE2A^Low/neg valves
disorganized alignment of PROX1^High cells

E *Pde2a^flox ; Prox1-CreER^T2* P11   PDE2A PROX1 CD31

fl/fl Cre-
CD31   PROX1   PDE2A

fl/fl Cre+

G *Pde2a^flox ; Prox1-CreER^T2* P11   CLDN5

fl/fl Cre-
valve sinus   total valve
valve sinus   total valve

fl/fl Cre+
valve sinus   total valve
valve sinus   total valve

(legend on next page)

junctions in the regions of collecting vessel valves, may also contribute to inherited, primary lymphedema.[12,63] Conversely, controlled disruption of lymphatic contact inhibition via PDE2A inhibition might also contribute to accelerated lymphatic regeneration, e.g., following LN dissection.

To our knowledge, PDE2A has not been implicated in LEC biology. The enzyme is extensively studied in the nervous system, where PDE2A inhibitors have emerged as a therapeutic approach to ameliorate cognitive dysfunction in neuropathological disorders, such as schizophrenia or Alzheimer disease.[64–66] However, all clinical trials studying PDE2A inhibitors have been unsuccessfully terminated, e.g., due to safety concerns.[65,67] In light of our findings, PDE2A inhibitors are likely to cause opposing effects depending on the cell type. Consequently, the identification of ubiquitously expressed molecules with multifaceted roles may also explain and can help avoid adverse effects of therapeutic drug targeting.

In summary, our study identifies the role of PDE2A in the lymphatic vasculature. PDE2A controls lymphatic contact inhibition and maturation through NOTCH activity in a cGMP- and p38-dependent manner.

STAR★METHODS

Detailed methods are provided in the online version of this paper and include the following:

- KEY RESOURCES TABLE
- RESOURCE AVAILABILITY
  - Lead contact
  - Materials availability
  - Data and code availability
- EXPERIMENTAL MODEL AND STUDY PARTICIPANT DETAILS
  - Animal models
  - Cell culture models
- METHOD DETAILS
  - Murine endothelial cell isolation
  - RNA interference
  - Cell growth on stiffness hydrogels
  - Bromodeoxyuridine (BrdU) incorporation assay
  - *in vitro* permeability assay
  - cAMP and cGMP incubation
  - cAMP/cGMP quantification
  - Phosphodiesterase activity assay
  - Notch activity assay
  - p38 inhibition assay
  - RNA sequencing
  - Immunofluorescence
  - Immunoprecipitation
  - Western blot
  - Flow cytometry
  - qRT-PCR analysis
  - microRNA expression analysis
  - Förster resonance energy transfer (FRET) measurements
  - Image acquisition
  - Image quantification
  - RNA single-cell sequencing data analysis
- QUANTIFICATION AND STATISTICAL ANALYSIS

SUPPLEMENTAL INFORMATION

Supplemental information can be found online at https://doi.org/10.1016/j.devcel.2023.12.002.

AUTHOR CONTRIBUTIONS

Conceptualization, M.F.; investigation, C.C., L.M.H.L., S.A.H., D.S., R.K., S.C., and M.F.; resources, T.E.S., M.P., V.O.N., T.R., and M.F.; writing—original draft, C.C. and M.F.; writing—review and editing, C.C., L.M.H.L., S.A.H., D.S., C. Saygi, R.K., S.C., J.K., C. Schulte, M.B., R.K.M., T.E.S., M.P., V.O.N., T.R., and M.F.; visualization, C.C., L.M.H.L., S.A.H., R.K., and M.F.; formal analysis, C. Saygi, J.K., C. Schulte, and M.F.; supervision, M.P., V.O.N., and M.F.; project administration, M.F.; funding acquisition, M.F.

Figure 7. Postnatal deletion of *Pde2a* results in abnormal mesenteric lymphatic valves

(A) Scheme of murine wild-type mesenteries and their vasculature. Lymph flow is directed from the gut toward the mesenteric lymph nodes (LNs). Lymphatic vessels arising from the gut have acquired pre-collecting lymphatic vessel identity (approximately 1/3 of vascular branch), whereas subsequent lymphatic vessels conduct lymph as part of the collecting lymphatic vessel network (approximately 2/3 of a vascular branch).[41]

(B) Whole-mount immunofluorescence staining of a wild-type P11 mesenteric lymphatic vessel stained with antibodies against PROX1 (red), CD31 (green), and PDE2A (magenta) showing highly enriched expression of PDE2A in valves of collecting LVs. Single channel images are shown for PDE2A and PROX1 in gray. Scale bars, 100 μm.

(C) Scheme of the genetic constructs and analyzed postnatal stage. Time points for 4-hydroxytamoxifen injections (Cre induction) are indicated.

(D) Quantification of LV diameter in P11 mesenteries of n = 2 KO and n = 2 CTRL embryos. Mean ± SEM, p value: unpaired Student's t test.

(E) Whole-mount immunofluorescence staining of P11 lymphatic valves of mesenteric collecting lymphatic vessels stained with antibodies against PROX1 (red), CD31 (green), and PDE2A (magenta). Scale bars, 100 μm.

(F) Quantification of valve number and morphology of collecting and large pre-collecting LVs in P11 mesenteries of n = 6 *Pde2a^{flox/flox}; Prox1-CreER^{T2}* mutant mice and n = 6 *Pde2a^{flox/flox}* control littermates.

(G) Whole-mount immunofluorescence staining of P11 lymphatic valves of mesenteric collecting lymphatic vessels stained with an antibody against CLDN5. Black arrows show jagged and discontinuous junctions. Scale bars, 50 μm.

REFERENCES

1. Zhang, F., Zarkada, G., Yi, S., and Eichmann, A. (2020). Lymphatic endothelial cell junctions: molecular regulation in physiology and diseases. Front. Physiol. 11, 509.

2. Szymborska, A., and Gerhardt, H. (2018). Hold me, but not too tight-endothelial cell-cell junctions in angiogenesis. Cold Spring Harb. Perspect. Biol. 10, a029223.

3. Potente, M., and Mäkinen, T. (2017). Vascular heterogeneity and specialization in development and disease. Nat. Rev. Mol. Cell Biol. 18, 477–494.

4. Choi, H.-J., Zhang, H., Park, H., Choi, K.-S., Lee, H.-W., Agrawal, V., Kim, Y.-M., and Kwon, Y.-G. (2015). Yes-associated protein regulates endothelial cell contact-mediated expression of angiopoietin-2. Nat. Commun. 6, 6943.

5. Lampugnani, M.G., Zanetti, A., Corada, M., Takahashi, T., Balconi, G., Breviario, F., Orsenigo, F., Cattelino, A., Kemler, R., Daniel, T.O., and Dejana, E. (2003). Contact inhibition of VEGF-induced proliferation requires vascular endothelial cadherin, β-catenin, and the phosphatase DEP-1/CD148. J. Cell Biol. 161, 793–804.

6. Baumeister, U., Funke, R., Ebnet, K., Vorschmitt, H., Koch, S., and Vestweber, D. (2005). Association of CSK to VE-cadherin and inhibition of cell proliferation. EMBO J. 24, 1686–1695.

7. Ritchey, L., Ha, T., Otsuka, A., Kabashima, K., Wang, D., Wang, Y., Lowy, D.R., and Tosato, G. (2019). DLC1 deficiency and YAP signaling drive endothelial cell contact inhibition of growth and tumorigenesis. Oncogene 38, 7046–7059.

8. Noseda, M., Chang, L., McLean, G., Grim, J.E., Clurman, B.E., Smith, L.L., and Karsan, A. (2004). Notch activation induces endothelial cell cycle arrest and participates in contact inhibition: role of p21Cip1 repression. Mol. Cell. Biol. 24, 8813–8822.

9. Oliver, G., Kipnis, J., Randolph, G.J., and Harvey, N.L. (2020). The lymphatic vasculature in the 21st century: novel functional roles in homeostasis and disease. Cell 182, 270–296.

10. Stritt, S., Koltowska, K., and Mäkinen, T. (2021). Homeostatic maintenance of the lymphatic vasculature. Trends Mol. Med. 27, 955–970.

11. Claesson-Welsh, L., Dejana, E., and McDonald, D.M. (2021). Permeability of the endothelial barrier: identifying and reconciling controversies. Trends Mol. Med. 27, 314–331.

12. Sabine, A., Bovay, E., Demir, C.S., Kimura, W., Jaquet, M., Agalarov, Y., Zangger, N., Scallan, J.P., Graber, W., Gulpinar, E., et al. (2015). FOXC2 and fluid shear stress stabilize postnatal lymphatic vasculature. J. Clin. Invest. 125, 3861–3877.

13. Surapisitchat, J., and Beavo, J.A. (2011). Regulation of endothelial barrier function by cyclic nucleotides: the role of phosphodiesterases. Handb. Exp. Pharmacol. 204, 193–210.

14. Dorland, Y.L., and Huveneers, S. (2017). Cell-cell junctional mechanotransduction in endothelial remodeling. Cell. Mol. Life Sci. 74, 279–292.

15. Gordon, E., Schimmel, L., and Frye, M. (2020). The importance of mechanical forces for in vitro endothelial cell biology. Front. Physiol. 11, 684.

16. Frye, M., Dierkes, M., Küppers, V., Vockel, M., Tomm, J., Zeuschner, D., Rossaint, J., Zarbock, A., Koh, G.Y., Peters, K., et al. (2015). Interfering with VE-PTP stabilizes endothelial junctions in vivo via Tie-2 in the absence of VE-cadherin. J. Exp. Med. 212, 2267–2287.

17. Hägerling, R., Hoppe, E., Dierkes, C., Stehling, M., Makinen, T., Butz, S., Vestweber, D., and Kiefer, F. (2018). Distinct roles of VE-cadherin for development and maintenance of specific lymph vessel beds. EMBO J. 37, e98271.

18. Frye, M., Stritt, S., Ortsäter, H., Hernandez Vasquez, M., Kaakinen, M., Vicente, A., Wiseman, J., Eklund, L., Martínez-Torrecuadrada, J.L., Vestweber, D., and Mäkinen, T. (2020). EphrinB2-EphB4 signalling provides Rho-mediated homeostatic control of lymphatic endothelial cell junction integrity. eLife 9, e57732.

19. Luxán, G., Stewen, J., Díaz, N., Kato, K., Maney, S.K., Aravamudhan, A., Berkenfeld, F., Nagelmann, N., Drexler, H.C., Zeuschner, D., et al. (2019). Endothelial EphB4 maintains vascular integrity and transport function in adult heart. eLife 8, e45863.

20. Weber, S., Zeller, M., Guan, K., Wunder, F., Wagner, M., and El-Armouche, A. (2017). PDE2 at the crossway between cAMP and cGMP signalling in the heart. Cell. Signal. 38, 76–84.

21. Surapisitchat, J., Jeon, K.I., Yan, C., and Beavo, J.A. (2007). Differential regulation of endothelial cell permeability by cGMP via phosphodiesterases 2 and 3. Circ. Res. 101, 811–818.

22. Chen, W., Spitzl, A., Mathes, D., Nikolaev, V.O., Werner, F., Weirather, J., Špiranec, K., Röck, K., Fischer, J.W., Kämmerer, U., et al. (2016). Endothelial actions of ANP enhance myocardial inflammatory infiltration in the early phase after acute infarction. Circ. Res. 119, 237–248.

23. Frye, M., Taddei, A., Dierkes, C., Martinez-Corral, I., Fielden, M., Ortsäter, H., Kazenwadel, J., Calado, D.P., Ostergaard, P., Salminen, M., et al. (2018). Matrix stiffness controls lymphatic vessel formation through regulation of a GATA2-dependent transcriptional program. Nat. Commun. 9, 1511.

24. Tabula Muris Consortium; Overall coordination; Logistical coordination; Organ collection and processing; Library preparation and sequencing; Computational data analysis; Cell type annotation; Writing group; Supplemental text writing group; Principal investigators (2018). Single-cell transcriptomics of 20 mouse organs creates a Tabula Muris. Nature 562, 367–372.

25. Assenza, M.R., Barbagallo, F., Barrios, F., Cornacchione, M., Campolo, F., Vivarelli, E., Gianfrilli, D., Auletta, L., Soricelli, A., Isidori, A.M., et al. (2018). Critical role of phosphodiesterase 2A in mouse congenital heart defects. Cardiovasc. Res. 114, 830–845.

26. Barbagallo, F., Rotilio, V., Assenza, M.R., Aguanno, S., Orsini, T., Putti, S., Isidori, A.M., Lenzi, A., Naro, F., De Angelis, L., and Pellegrini, M. (2020). PDE2A is indispensable for mouse liver development and hematopoiesis. Int. J. Mol. Sci. 21, 2902.

27. Stephenson, D.T., Coskran, T.M., Kelly, M.P., Kleiman, R.J., Morton, D., O'Neill, S.M., Schmidt, C.J., Weinberg, R.J., and Menniti, F.S. (2012). The distribution of phosphodiesterase 2A in the rat brain. Neuroscience 226, 145–155.

28. Burger, N.B., Bekker, M.N., Kok, E., De Groot, C.J., Martin, J.F., Shou, W., Scambler, P.J., Lee, Y., Christoffels, V.M., and Haak, M.C. (2015). Increased nuchal translucency origins from abnormal lymphatic development and is independent of the presence of a cardiac defect. Prenat. Diagn. 35, 1278–1286.

29. Beese, M., Wyss, K., Haubitz, M., and Kirsch, T. (2010). Effect of cAMP derivates on assembly and maintenance of tight junctions in human umbilical vein endothelial cells. BMC Cell Biol. 11, 68.

30. Waschke, J., Drenckhahn, D., Adamson, R.H., Barth, H., and Curry, F.E. (2004). cAMP protects endothelial barrier functions by preventing Rac-1 inhibition. Am. J. Physiol. Heart Circ. Physiol. 287, H2427–H2433.

31. Fu, B.M., Yang, J., Cai, B., Fan, J., Zhang, L., and Zeng, M. (2015). Reinforcing endothelial junctions prevents microvessel permeability increase and tumor cell adhesion in microvessels in vivo. Sci. Rep. 5, 15697.

32. Perrot, C.Y., Sawada, J., and Komatsu, M. (2018). Prolonged activation of cAMP signaling leads to endothelial barrier disruption via transcriptional repression of RRAS. FASEB J. 32, fj201700818RRR.

33. Breslin, J.W. (2011). ROCK and cAMP promote lymphatic endothelial cell barrier integrity and modulate histamine and thrombin-induced barrier dysfunction. Lymphat. Res. Biol. 9, 3–11.

34. Price, G.M., Chrobak, K.M., and Tien, J. (2008). Effect of cyclic AMP on barrier function of human lymphatic microvascular tubes. Microvasc. Res. *76*, 46–51.

35. Zaccolo, M., and Movsesian, M.A. (2007). cAMP and cGMP signaling cross-talk: role of phosphodiesterases and implications for cardiac pathophysiology. Circ. Res. *100*, 1569–1578.

36. Conti, M., and Beavo, J. (2007). Biochemistry and physiology of cyclic nucleotide phosphodiesterases: essential components in cyclic nucleotide signaling. Annu. Rev. Biochem. *76*, 481–511.

37. Browning, D.D., McShane, M.P., Marty, C., and Ye, R.D. (2000). Nitric oxide activation of p38 mitogen-activated protein kinase in 293T fibroblasts requires cGMP-dependent protein kinase. J. Biol. Chem. *275*, 2811–2816.

38. Li, Z., Zhang, G., Feil, R., Han, J., and Du, X. (2006). Sequential activation of p38 and ERK pathways by cGMP-dependent protein kinase leading to activation of the platelet integrin αIIbβ3. Blood *107*, 965–972.

39. Matsumoto, T., Turesson, I., Book, M., Gerwins, P.r., and Claesson-Welsh, L. (2002). p38 MAP kinase negatively regulates endothelial cell survival, proliferation, and differentiation in FGF-2–stimulated angiogenesis. J. Cell Biol. *156*, 149–160.

40. Zhang, Y., Ulvmar, M.H., Stanczuk, L., Martinez-Corral, I., Frye, M., Alitalo, K., and Mäkinen, T. (2018). Heterogeneity in VEGFR3 levels drives lymphatic vessel hyperplasia through cell-autonomous and non-cell-autonomous mechanisms. Nat. Commun. *9*, 1296.

41. Sabine, A., Davis, M.J., Bovay, E., and Petrova, T.V. (2018). Characterization of mouse mesenteric lymphatic valve structure and function. Methods Mol. Biol. *1846*, 97–129.

42. Hilfenhaus, G., Nguyen, D.P., Freshman, J., Prajapati, D., Ma, F., Song, D., Ziyad, S., Cuadrado, M., Pellegrini, M., Bustelo, X.R., and Iruela-Arispe, M.L. (2018). Vav3-induced cytoskeletal dynamics contribute to heterotypic properties of endothelial barriers. J. Cell Biol. *217*, 2813–2830.

43. Richards, M., Nwadozi, E., Pal, S., Martinsson, P., Kaakinen, M., Gloger, M., Sjöberg, E., Koltowska, K., Betsholtz, C., Eklund, L., et al. (2022). Claudin5 protects the peripheral endothelial barrier in an organ and vessel-type-specific manner. eLife *11*, e78517.

44. Favot, L., Keravis, T., Holl, V., Le Bec, A., and Lugnier, C. (2003). VEGF-induced HUVEC migration and proliferation are decreased by PDE2 and PDE4 inhibitors. Thromb. Haemost. *90*, 334–343.

45. Scallan, J.P., Hill, M.A., and Davis, M.J. (2015). Lymphatic vascular integrity is disrupted in type 2 diabetes due to impaired nitric oxide signalling. Cardiovasc. Res. *107*, 89–97.

46. Kimura, T., Hamazaki, T.S., Sugaya, M., Fukuda, S., Chan, T., Tamura-Nakano, M., Sato, S., and Okochi, H. (2014). Cilostazol improves lymphatic function by inducing proliferation and stabilization of lymphatic endothelial cells. J. Dermatol. Sci. *74*, 150–158.

47. Sweet, D.T., Jiménez, J.M., Chang, J., Hess, P.R., Mericko-Ishizuka, P., Fu, J., Xia, L., Davies, P.F., and Kahn, M.L. (2015). Lymph flow regulates collecting lymphatic vessel maturation in vivo. J. Clin. Invest. *125*, 2995–3007.

48. Murtomaki, A., Uh, M.K., Choi, Y.K., Kitajewski, C., Borisenko, V., Kitajewski, J., and Shawber, C.J. (2013). Notch1 functions as a negative regulator of lymphatic endothelial cell differentiation in the venous endothelium. Development *140*, 2365–2376.

49. Zheng, W., Tammela, T., Yamamoto, M., Anisimov, A., Holopainen, T., Kaijalainen, S., Karpanen, T., Lehti, K., Ylä-Herttuala, S., and Alitalo, K. (2011). Notch restricts lymphatic vessel sprouting induced by vascular endothelial growth factor. Blood *118*, 1154–1162.

50. Niessen, K., Zhang, G., Ridgway, J.B., Chen, H., Kolumam, G., Siebel, C.W., and Yan, M. (2011). The Notch1-Dll4 signaling pathway regulates mouse postnatal lymphatic development. Blood *118*, 1989–1997.

51. Fatima, A., Culver, A., Culver, F., Liu, T., Dietz, W.H., Thomson, B.R., Hadjantonakis, A.K., Quaggin, S.E., and Kume, T. (2014). Murine Notch1 is required for lymphatic vascular morphogenesis during development. Dev. Dyn. *243*, 957–964.

52. Shen, W., Huang, J., and Wang, Y. (2021). Biological significance of NOTCH signaling strength. Front. Cell Dev. Biol. *9*, 652273.

53. Li, J., Li, Q., Lin, L., Wang, R., Chen, L., Du, W., Jiang, C., and Li, R. (2018). Targeting the Notch1 oncogene by miR-139-5p inhibits glioma metastasis and epithelial-mesenchymal transition (EMT). BMC Neurol. *18*, 133.

54. Watanabe, K., Amano, Y., Ishikawa, R., Sunohara, M., Kage, H., Ichinose, J., Sano, A., Nakajima, J., Fukayama, M., Yatomi, Y., et al. (2015). Histone methylation-mediated silencing of miR-139 enhances invasion of non-small-cell lung cancer. Cancer Med. *4*, 1573–1582.

55. Geng, X., Yanagida, K., Akwii, R.G., Choi, D., Chen, L., Ho, Y., Cha, B., Mahamud, M.R., Berman de Ruiz, K., Ichise, H., et al. (2020). S1PR1 regulates the quiescence of lymphatic vessels by inhibiting laminar shear stress–dependent VEGF-C signaling. JCI Insight *5*, e137652.

56. Mukohda, M., Mizuno, R., and Ozaki, H. (2020). Increased blood pressure causes lymphatic endothelial dysfunction via oxidative stress in spontaneously hypertensive rats. Hypertension *76*, 598–606.

57. Corre, I., Paris, F., and Huot, J. (2017). The p38 pathway, a major pleiotropic cascade that transduces stress and metastatic signals in endothelial cells. Oncotarget *8*, 55684–55714.

58. Saygili Demir, C., Sabine, A., Gong, M., Dormond, O., and Petrova, T.V. (2023). Mechanosensitive mTORC1 signaling maintains lymphatic valves. J. Cell Biol. *222*, e202207049.

59. Baluk, P., Fuxe, J., Hashizume, H., Romano, T., Lashnits, E., Butz, S., Vestweber, D., Corada, M., Molendini, C., Dejana, E., and McDonald, D.M. (2007). Functionally specialized junctions between endothelial cells of lymphatic vessels. J. Exp. Med. *204*, 2349–2362.

60. Fonseca, D.M., Hand, T.W., Han, S.J., Gerner, M.Y., Glatman Zaretsky, A., Byrd, A.L., Harrison, O.J., Ortiz, A.M., Quinones, M., Trinchieri, G., et al. (2015). Microbiota-dependent sequelae of acute infection compromise tissue-specific immunity. Cell *163*, 354–366.

61. Ivanov, S., Scallan, J.P., Kim, K.W., Werth, K., Johnson, M.W., Saunders, B.T., Wang, P.L., Kuan, E.L., Straub, A.C., Ouhachi, M., et al. (2016). CCR7 and IRF4-dependent dendritic cells regulate lymphatic collecting vessel permeability. J. Clin. Invest. *126*, 1581–1591.

62. Kuan, E.L., Ivanov, S., Bridenbaugh, E.A., Victora, G., Wang, W., Childs, E.W., Platt, A.M., Jakubzick, C.V., Mason, R.J., Gashev, A.A., et al. (2015). Collecting lymphatic vessel permeability facilitates adipose tissue inflammation and distribution of antigen to lymph node-homing adipose tissue dendritic cells. J. Immunol. *194*, 5200–5210.

63. Mahamud, M.R., Geng, X., Ho, Y.C., Cha, B., Kim, Y., Ma, J., Chen, L., Myers, G., Camper, S., Mustacich, D., et al. (2019). GATA2 controls lymphatic endothelial cell junctional integrity and lymphovenous valve morphogenesis through miR-126. Development *146*, dev184218.

64. Mikami, S., Nakamura, S., Ashizawa, T., Nomura, I., Kawasaki, M., Sasaki, S., Oki, H., Kokubo, H., Hoffman, I.D., Zou, H., et al. (2017). Discovery of clinical candidate N-((1S)-1-(3-Fluoro-4-(trifluoromethoxy)phenyl)-2-methoxyethyl)-7-methoxy-2-oxo-2,3-dihydropyrido[2,3-b]pyrazine-4(1H)-carboxamide (TAK-915): a highly potent, selective, and brain-penetrating phosphodiesterase 2a inhibitor for the treatment of cognitive disorders. J. Med. Chem. *60*, 7677–7702.

65. Baillie, G.S., Tejeda, G.S., and Kelly, M.P. (2019). Therapeutic targeting of 3′,5′-cyclic nucleotide phosphodiesterases: inhibition and beyond. Nat. Rev. Drug Discov. *18*, 770–796.

66. Delhaye, S., and Bardoni, B. (2021). Role of phosphodiesterases in the pathophysiology of neurodevelopmental disorders. Mol. Psychiatry *26*, 4570–4582.

67. Trabanco, A.A., Buijnsters, P., and Rombouts, F.J. (2016). Towards selective phosphodiesterase 2A (PDE2A) inhibitors: a patent review (2010 - present). Expert Opin. Ther. Pat. *26*, 933–946.

68. Bork, N.I., Kuret, A., Cruz Santos, M., Molina, C.E., Reiter, B., Reichenspurner, H., Friebe, A., Skryabin, B.V., Rozhdestvensky, T.S., Kuhn, M., et al. (2021). Rise of cGMP by partial phosphodiesterase-3A degradation enhances cardioprotection during hypoxia. Redox Biol. *48*, 102179.

69. Kisanuki, Y.Y., Hammer, R.E., Miyazaki, J., Williams, S.C., Richardson, J.A., and Yanagisawa, M. (2001). Tie2-Cre transgenic mice: a new model for endothelial cell-lineage analysis in vivo. Dev. Biol. *230*, 230–242.

70. Sörensen, I., Adams, R.H., and Gossler, A. (2009). DLL1-mediated Notch activation regulates endothelial identity in mouse fetal arteries. Blood *113*, 5680–5688.

71. Bazigou, E., Lyons, O.T.A., Smith, A., Venn, G.E., Cope, C., Brown, N.A., and Makinen, T. (2011). Genes regulating lymphangiogenesis control venous valve formation and maintenance in mice. J. Clin. Invest. *121*, 2984–2992.

72. Satija, R., Farrell, J.A., Gennert, D., Schier, A.F., and Regev, A. (2015). Spatial reconstruction of single-cell gene expression data. Nat. Biotechnol. *33*, 495–502.

73. McInnes, L., Healy, J., Saul, N., and Großberger, L. (2018). UMAP: uniform manifold approximation and projection. J. Open Source Software *3*, 861.

74. Bolger, A.M., Lohse, M., and Usadel, B. (2014). Trimmomatic: a flexible trimmer for Illumina sequence data. Bioinformatics *30*, 2114–2120.

75. Dobin, A., Davis, C.A., Schlesinger, F., Drenkow, J., Zaleski, C., Jha, S., Batut, P., Chaisson, M., and Gingeras, T.R. (2013). STAR: ultrafast universal RNA-seq aligner. Bioinformatics *29*, 15–21.

76. Zhang, Y., Parmigiani, G., and Johnson, W.E. (2020). ComBat-seq: batch effect adjustment for RNA-seq count data. NAR Genom. Bioinform. *2*, lqaa078.

77. Liao, Y., Wang, J., Jaehnig, E.J., Shi, Z., and Zhang, B. (2019). WebGestalt 2019: gene set analysis toolkit with revamped UIs and APIs. Nucleic Acids Res. *47*, W199–W205.

78. Rodríguez, C.I., Buchholz, F., Galloway, J., Sequerra, R., Kasper, J., Ayala, R., Stewart, A.F., and Dymecki, S.M. (2000). High-efficiency deleter mice show that FLPe is an alternative to Cre-loxP. Nat. Genet. *25*, 139–140.

79. Zink, J., Frye, M., Frömel, T., Carlantoni, C., John, D., Schreier, D., Weigert, A., Laban, H., Salinas, G., Stingl, H., et al. (2021). EVL regulates VEGF receptor-2 internalization and signaling in developmental angiogenesis. EMBO Rep. *22*, e48961.

80. Tse, J.R., and Engler, A.J. (2010). Preparation of hydrogel substrates with tunable mechanical properties. Curr. Protoc. Cell Biol. *Chapter 10*. Unit 10.16.

81. Thompson, W.J., and Appleman, M.M. (1971). Multiple cyclic nucleotide phosphodiesterase activities from rat brain. Biochemistry *10*, 311–316.

82. Love, M.I., Huber, W., and Anders, S. (2014). Moderated estimation of fold change and dispersion for RNA-seq data with DESeq2. Genome Biol. *15*, 550.

83. Wong, L., Lee, K., Russell, I., and Chen, C.. Endogenous controls for real-time quantitation of mirna using TaqMan® MicroRNA assays. Applied Biosystems Application Note. https://www.gene-quantification.de/AB-microRNA-endog-controls.pdf.

84. Perera, R.K., Sprenger, J.U., Steinbrecher, J.H., Hübscher, D., Lehnart, S.E., Abesser, M., Schuh, K., El-Armouche, A., and Nikolaev, V.O. (2015). Microdomain switch of cGMP-regulated phosphodiesterases leads to ANP-induced augmentation of β-adrenoceptor-stimulated contractility in early cardiac hypertrophy. Circ. Res. *116*, 1304–1311.

85. Börner, S., Schwede, F., Schlipp, A., Berisha, F., Calebiro, D., Lohse, M.J., and Nikolaev, V.O. (2011). FRET measurements of intracellular cAMP concentrations and cAMP analog permeability in intact cells. Nat. Protoc. *6*, 427–438.

STAR★METHODS

KEY RESOURCES TABLE

REAGENT or RESOURCE	SOURCE	IDENTIFIER
Antibodies		
Goat polyclonal anti-PROX1	R&D Systems	Cat# AF2727; RRID:AB_2170716
Goat polyclonal anti-VE-cadherin (clone C19)	Santa Cruz Biotechnologies	Cat# sc-6458; RRID:AB_2077955
Goat polyclonal anti-NRP2	R&D Systems	Cat# AF567; RRID:AB_2155253
Goat polyclonal anti-VE-cadherin	R&D Systems	Cat# AF1002; RRID:AB_2077789
Goat polyclonal anti-VEGFR3	R&D Systems	Cat# AF743; RRID:AB_355563
Hamster monoclonal anti-PDPN-APC (clone 8.1.1)	Biolegend	Cat# 127410; RRID:AB_10612940
Mouse anti-BrdU	BD Biosciences	Cat# 347580; RRID:AB_10015219
Rabbit anti-PDE3A	Bork et al.[68]	N/A
Mouse monoclonal anti-CD31-PE-Cy7 (clone 390)	Invitrogen eBioscience	Cat# 25-0311-82; RRID:AB_2716949
Mouse monoclonal anti-PDE2A	Santa Cruz Biotechnologies	Cat# sc-271394; RRID:AB_10610755
Mouse monoclonal anti-VE-cadherin (clone F8)	Santa Cruz Biotechnologies	Cat# sc-9989; RRID:AB_2077957
Mouse monoclonal anti-VEGFR3	Millipore	Cat# MAB3757; RRID:AB_11210795
Mouse monoclonal anti-αSMA-cy3	Sigma Aldrich	Cat# C6198; RRID:AB_476856
Mouse monoclonal anti-phosphotyrosine (4G10 clone)	Millipore	Cat# 05-321; RRID:AB_2891016
Rabbit monoclonal anti-cleaved Notch1	Cell Signaling	Cat# 4147; RRID:AB_2153348
Rabbit monoclonal anti-Ki67	Abcam	Cat# ab16667; RRID:AB_302459
Rabbit monoclonal anti-β-actin	Cell Signaling	Cat# 4970; RRID:AB_2223172
Rabbit polyclonal anti-p38 MAPK	Cell Signaling	Cat# 9212; RRID:AB_330713
Rabbit polyclonal anti-phospho-p38 MAPK	Cell Signaling	Cat# 9211; RRID:AB_331641
Rabbit polyclonal anti-VE-cadherin	Proteintech	Cat# 27956-1-AP; RRID:AB_2918136
Rabbit polyclonal anti-CLDN5	Thermo Fischer Scientific	Cat# 34–1600; RRID:AB_86930
Rabbit polyclonal anti-LYVE1	Relia Tech GmbH	Cat# 103-PA50AG; RRID:AB_2876870
Rat anti-CD16/CD32 (Mouse BD Fc Block™, Clone 2.4G2)	BD Biosciences	Cat# 553141; RRID:AB_394656
Rat monoclonal anti-CD11b-eF450	Invitrogen eBioscience	Cat# 48-0112-82; RRID:AB_1582236
Rat monoclonal anti-CD31 (clone Mec13.3)	BioLegend	Cat# 102501; RRID:AB_312908
Rat monoclonal anti-CD45-eF450	Invitrogen eBioscience	Cat# 48-0451-82; RRID:AB_1518806
Rat monoclonal anti-Endomucin	Santa Cruz Biotechnologies	Cat# sc-65495; RRID:AB_2100037
Rat monoclonal anti-Ter119-eF450	Invitrogen eBioscience	Cat# 48-5921-82; RRID:AB_1518808
Alexa Fluor® 488 donkey anti-goat	Jackson ImmunoResearch Labs	Cat# 705-545-003; RRID:AB_2340428
Alexa Fluor® 594 donkey anti-goat	Jackson ImmunoResearch Labs	Cat# 705-585-003; RRID:AB_2340432
Alexa Fluor® 647 donkey anti-goat	Jackson ImmunoResearch Labs	Cat# 705-605-003; RRID:AB_2340436
Alexa Fluor® 488 donkey anti-rat	Jackson ImmunoResearch Labs	Cat# 712-545-153; RRID:AB_2340684
Alexa Fluor® 594 donkey anti-rat	Jackson ImmunoResearch Labs	Cat# 712-585-153; RRID:AB_2340689
Alexa Fluor® 647 donkey anti-rat	Jackson ImmunoResearch Labs	Cat# 712-605-153; RRID:AB_2340694
Alexa Fluor® 488 donkey anti-mouse	Jackson ImmunoResearch Labs	Cat# 715-545-151; RRID:AB_2341099
Alexa Fluor® 594 donkey anti-mouse	Jackson ImmunoResearch Labs	Cat# 715-585-151; RRID:AB_2340855
Alexa Fluor® 647 donkey anti-mouse	Jackson ImmunoResearch Labs	Cat# 715-605-151; RRID:AB_2340863
Alexa Fluor® 488 donkey anti-rabbit	Jackson ImmunoResearch Labs	Cat# 711-545-152; RRID:AB_2313584
Alexa Fluor® 594 donkey anti-rabbit	Jackson ImmunoResearch Labs	Cat# 711-585-152; RRID:AB_2340621

Continued

REAGENT or RESOURCE	SOURCE	IDENTIFIER
Alexa Fluor® 647 donkey anti-rabbit	Jackson ImmunoResearch Labs	Cat# 711-605-152; RRID:AB_2492288
Peroxidase-conjugated IgG Fraction monoclonal mouse anti-goat	Jackson ImmunoResearch Labs	Cat# 205-032-176; RRID:AB_2339056
Polyclonal rabbit anti-mouse immunoglobulins/HRP	Agilent	Cat# P0260; RRID:AB_2636929
Polyclonal goat anti-rabbit immunoglobulins/HRP	Agilent	Cat# P0448; RRID:AB_2617138)
Biological samples		
E13.4 mouse embryos	This manuscript	N/A
E14.5 mouse embryos	This manuscript	N/A
E16.5 mouse embryos	This manuscript	N/A
E17.5 mouse embryos	This manuscript	N/A
P11 mouse mesenteries	This manuscript	N/A
Lungs from 12-week-old mice	This manuscript	N/A
Chemicals, peptides, and recombinant proteins		
0.05% Trypsin/EDTA	Gibco	Cat# 25300-054
2-mercaptoethanol	Carl Roth GmbH	Cat 4227.1
3-Aminopropyltriethoxysilane	Sigma-Aldrich	Cat# 440140
[3H] cGMP	PerkinElmer	Cat# NET337250UC
4-hydroxytamoxifen	Sigma-Aldrich	Cat# H7904
8-Br-cAMP	Sigma-Aldrich	Cat# B5386
8-Br-cGMP	Sigma-Aldrich	Cat# B1381
Acrylamide 40%	Sigma-Aldrich	Cat# A4058-100ML
Alexa Fluor™ 488 Phalloidin	Thermo Fisher Scientific	Cat# A12379
Alexa Fluor™ 594 Phalloidin	Thermo Fisher Scientific	Cat# A12381
ANP1-28 (human)	Calbiochem	Cat# 05-23-0300
Antiprotease cocktail	Sigma-Aldrich	Cat# P8340
BIS-Acrylamide	Sigma-Aldrich	Cat# M1533-100ML
Bovine brain extract (BBE)	Lonza BioScience	Cat#: CC-4098
Bovine serum albumin	Sigma-Aldrich	Cat# A3294
BAY60-7550	Santa Cruz	Cat# sc396772
Bovine fibronectin	Sigma-Aldrich	Cat# F1141-1MG
BrdU	BD Biosciences	Cat# 550891
Cilostamide	Santa Cruz	Cat# sc201180A
Collagen I	Gibco	Cat# A10483-01
Collagenase A	Roche	Cat# 10103586001
Collagenase type IV	Gibco	Cat# 17104-019
DAPT	Abcam	Cat# 208255-80-5
Dichlordimethylsilane	Sigma	Cat# 440272
DMEM	Gibco	Cat#: 41966-029
Dnase I	Roche	Cat# 10104159001
Dulbecco's phosphate buffered saline (PBS)	R&D Systems	Cat#: F1141
EGTA	Sigma-Aldrich	Cat# 03777
Endothelial Cell Growth Medium (ECGM)	PromoCell	Cat# C-22010
Endothelial Cell Growth Medium MV2 (ECGMV2)	PromoCell	Cat# C-22022
Fetal bovine serum (FBS)	Gibco	Cat# 10500-064
FITC-dextran (40kDa)	Sigma-Aldrich	Cat# FD40S
Fluoroshield Mounting Medium with DAPI	Sigma-Aldrich	Cat# F6057

Continued

REAGENT or RESOURCE	SOURCE	IDENTIFIER
Fluoroshield Mounting Medium without DAPI	Sigma-Aldrich	Cat# F6182
FSK	Hello Bio	Cat# HB1348-10MG
Hepes	Sigma-Aldrich	Cat# H3375
Human ANP	Bachem	Cat# 4011941
Human sDLL4	Sigma Aldrich	Cat# SRP3026
IBMX	Applichem	Cat# A0695-0001
Isoprenaline	Sigma Aldrich	Cat# I6504
Laemmli Sample Buffer 4x	BioRad	Cat# 1510747
Lipofectamine 3000	Invitrogen	Cat# L3000015
MEM NEAA (Non-Essential Amino Acid) 100X	Gibco	Cat# 11140-050
OptiMEM Reduced Serum Medium	Gibco	Cat# 31985-062
PageRuler™ Prestained Protein Ladder	Thermo Fisher Scientific	Cat# 26616
Penicillin-Streptomycin (10,000 U/mL)	Gibco	Cat# 15140122
Pierce™ Protease Inhibitor Mini Tablets, EDTA-free	Thermo Fisher Scientific	Cat# A32955
Protein G Sepharose™ Fast Flow	Sigma-Aldrich	Cat# P3296
SB203580	Sigma Aldrich	Cat# S8307
Soybean trypsin inhibitor	Sigma Aldrich	Cat# T6522
Snake venom from Crotalus atrox	Sigma Aldrich	Cat# V7000
Sulpho-SANPAH	Sigma	Cat# 803332
SytoxBlue	Invitrogen	Cat# S34857
Tamoxifen	Sigma-Aldrich	Cat# T5648
Tween® 20	Sigma-Aldrich	Cat# P1379
Triton X-100	BioRad	Cat# 1610407
VEGF-C	R&D Systems	Cat# 9199-VC
Critical commercial assays		
Alexa Fluor™ 555 Tyramide SuperBoost™ Kit	Thermo Fisher Scientific	Cat# B40923
BGI Plug-In Adapter Kit	BGI	Cat# LA00R04
blackPREP Rodent Tail DNA Kit	IST Innuscreen GmbH	Cat# 845-BP-0010010
Direct cAMP ELISA Kit	Enzo Life Science, Inc.	Cat# ADI-900-066
Direct cGMP ELISA Kit	Enzo Life Science, Inc.	Cat# ADI-900-014
ECL™ Select Western Blotting Detection Reagent	Cytiva	Cat# RPN2235
miRNeasy Mini Kit	Qiagen	Cat# 217004
Optimal Dual-mode mRNA Library Prep Kit	BGI	Cat# LR00R96
Pierce™ BCA Protein Assay Kit	Thermo Fisher Scientific	Cat# 23225
TaqMan™ PreAmp Master Mix	Applied Biosystems	Cat# 4391128
Rneasy® Micro Kit	Qiagen	Cat# 74004
Rneasy® Mini Kit	Qiagen	Cat# 74104
SuperScript® IV VILO cDNA Synthesis Kit	Thermo Fisher Scientific	Cat# 11754050
TaqMan™ Gene Expression Assay	Applied Biosystems	Cat# 4369016
TaqMan™ MicroRNA Assay	Thermo Fisher Scientific	Cat# 4427975
TaqMan™ MicroRNA Reverse Transcription Kit	Thermo Fisher Scientific	Cat# 4366596
TaqMan™ Universal Master Mix II no UNG	Thermo Fisher Scientific	Cat# 4440043
Deposited data		
Bulk RNA sequencing datasets	European Nucleotide Archive (ENA)	Accession number: PRJEB57972
Original western blot images/ source data	Mendeley data	https://doi.org/10.17632/mmz2gznth5.1

(Continued on next page)

Continued

REAGENT or RESOURCE	SOURCE	IDENTIFIER
Experimental models: Cell lines		
HDLECs	PromoCell	Cat# C-12216
HUVECs	PromoCell	Cat# C-12203
mECs	This manuscript	N/A
Experimental models: Organisms/strains		
Mouse: *Tie2-Cre* (B6.Cg-Tg(Tek-cre) 1Ywa/J)	Kisanuki et al.[69]	RRID:IMSR_JAX:008863
Mouse: *Cdh5-CreER^T2* (Tg(Cdh5-cre/ ERT2)1Rha)	Sörensen et al.[70]	RRID:IMSR_EM:14891
Mouse: *Prox1-CreER^T2* (Tg(Prox1-cre/ ERT2)1Tmak	Bazigou et al.[71]	RRID:IMSR_EM:13737
Mouse: *Pde2a* global knockout (B6; 129P2-487Pde2A < tm1Dgen>/H; EM: 02366)	Assenza et al.[25]	RRID:IMSR_EM:02366
Mouse: *Pde2a* (Pde2a^tm1a(EUCOMM)Wtsl)	This manuscript	N/A
Oligonucleotides		
AllStars Negative CTRL siRNA	Qiagen	Cat# 1027281
FlexiTube *PDE2A* siRNA	Qiagen	Cat# SI00040159
DLL1 (hs00194509_m1)	Thermo Fischer Scientific	Cat# 4331182
GAPDH (hs99999905)	Thermo Fischer Scientific	Cat# 4326317E
Gapdh (mm99999915_g1)	Thermo Fischer Scientific	Cat# 4352932E
GJA4 (hs00704917_s1)	Thermo Fischer Scientific	Cat# 4331182
Hey1 (mm00468865_m1)	Thermo Fischer Scientific	Cat# 4331182
miR-139-5p (MI0000693)	Thermo Fischer Scientific	Cat# 002289
Mki67 (mm01278617_m1)	Thermo Fischer Scientific	Cat# 4331182
PDE10A (hs01098928_m1)	Thermo Fischer Scientific	Cat# 4351372
PDE12 (hs00698272_m1)	Thermo Fischer Scientific	Cat# 4331182
PDE2A (hs00159935_m1)	Thermo Fischer Scientific	Cat# 4331182
Pde2a (mm01136644_m1)	Thermo Fischer Scientific	Cat# 4331182
PDE3A (hs01012698_m1)	Thermo Fischer Scientific	Cat# 4331182
PDE4B (hs00963643_m1)	Thermo Fischer Scientific	Cat# 4331182
PDE4D (hs01579625_m1)	Thermo Fischer Scientific	Cat# 4331182
PDE6D (hs01062025_m1)	Thermo Fischer Scientific	Cat# 4331182
PDE8A (hs01079617_m1)	Thermo Fischer Scientific	Cat# 4331182
PSEN2 (hs01577197_m1)	Thermo Fischer Scientific	Cat# 4331182
RNU48 (TaqMan™ MicroRNA Assay)	Thermo Fischer Scientific	Cat# 001006
snoRNA202 (TaqMan™ MicroRNA Assay)	Thermo Fischer Scientific	Cat# 001232
snoRNA234 (TaqMan™ MicroRNA Assay)	Thermo Fischer Scientific	Cat# 001234
Pde2a-5'-arm 5'ACTGGTCAGTTCTGAGC CTCACCC 3'	This paper	N/A
Pde2a-3'-arm 5' AGTCTGGACTCCCCA TCTAGCAGG 3'	This paper	N/A
Cre transgene sense 5'GAACCTGATGG ACATGTTCAGG 3'	This paper	N/A
Cre transgene antisense 5' AGTGCGTT CGAACGCTAGAGCCTGT 3'	This paper	N/A
Myogenin sense 5' TTACGTCCA TCGTGGACAGC 3'	This paper	N/A
Myogenin antisense 5' TGGGCTGGGT GTTAGCCTTA 3'	This paper	N/A

(Continued on next page)

Continued

REAGENT or RESOURCE	SOURCE	IDENTIFIER
Software and algorithms		
BioRad Image Lab Software	BioRad	N/A
Diva 8.0.1 software	BD Biosciences	N/A
Fiji ImageJ	N/A	https://imagej.net/ij/
GraphPad Prism 9	Dotmatics	N/A
Leica LAS-X software	Leica	N/A
MicroManager 1.4 software	Open source	N/A
Seurat package	Satija et al.[72]	https://www.nature.com/articles/nbt.3192
umap package	McInnes et al.[73]	https://joss.theoj.org/papers/10.21105/joss.00861
Plotly software	Open source	https://plotly.com/r/
FastQC (v0.11.9)	Open source	http://www.bioinformatics.babraham.ac.uk/projects/fastqc/
Trimmomatic (v0.36)	Bolger et al.[74]	https://academic.oup.com/bioinformatics/article/30/15/2114/2390096?login=true
STAR (v2.7.3a)	Dobin et al.[75]	https://academic.oup.com/bioinformatics/article/29/1/15/272537
ComBat-seq	Zhang et al.[76]	https://academic.oup.com/nargab/article/2/3/lqaa078/5909519?searchresult=1
WebGestalt platform 2019	Liao et al.[77]	https://academic.oup.com/nar/article/47/W1/W199/5494758?login=true
Other		
24-well Plate Softwell Easy Coat hydrogels (0.1, 1, 2, 4 and 25kPa)	Matrigen	Cat# SS24-EC
8-well Lab-Tek II chamber slides	Lab-Tek®	Cat# 154941
Agilent Technologies 2100 bioanalyzer	Agilent	https://www.agilent.com/en/product/automated-electrophoresis/bioanalyzer-systems/bioanalyzer-instrument
AMPure® XP magnetic beads	Beckman	Cat# A53880
Axiocam 208 Color	Zeiss	N/A
BD Biosciences FACSAria™IIIu	BD Biosciences	N/A
CoolLED beam-splitter DV2 Dual View	Photometrics	N/A
CMOS camera chip	OptiMOS, Qimaging	N/A
DEAE-Sephadex A-25 columns	Cytiva	Cat# 17017001
DynaMag™-2	Invitrogen	Cat# 12321D
Gel Doc™ MP Imaging System	BioRad	N/A
Hamilton® TLC syringe	Sigma-Aldrich	Cat# HAM7635-01-1EA
Immobilion®-P Transfer Membrane (0.45μm pore size)	Merck	Cat# IPVH00010
Inject®-F syringe	Braun	Cat# 9166017V
Leica DMI 3000 B inverted fluorescent microscope	Leica	N/A
Leica SP8 inverted microscope	Leica	N/A
Nikon Eclipse Ts2R microscope	Nikon	N/A
Sheep-anti-rat IgG Dynabeads™	Invitrogen	Cat# 110-35
StepOnePlus RT PCR system	Applied Biosystems	N/A
Tecan Spark® 10M microplate reader	Tecan	N/A
Tissue culture-treated dishes	Corning	Cat# 430167
Tissue culture-treated dishes (60mm)	Corning	Cat# 430166
Transwell filters (0.4μm pore size)	Corning	Cat# 3413

(Continued on next page)

Continued

REAGENT or RESOURCE	SOURCE	IDENTIFIER
Tri-Carb 2100TR Liquid Scintillation Counter	Packard Instruments	Cat# 2000CA
ULTIMA GOLD scintillation liquid	PerkinElmer	Cat# 6013326
UltraComp eBeads Plus Compensation Beads	Invitrogen	Cat# 01-3333-42
Zeiss Stemi 508	Zeiss	N/A

RESOURCE AVAILABILITY

Lead contact
Further information and requests for resources and reagents should be directed to and will be fulfilled by the lead contact, Prof. Maike Frye (m.frye@uke.de).

Materials availability
ES cell line containing 'knockout-first' Pde2a allele (Pde2a^tm1a(EUCOMM)Wtsi) is available from the European Conditional Mouse Mutagenesis Program (EUCOMM).

Data and code availability
The authors declare that the data supporting the findings of this study are available within the paper and its supplementary information. Bulk RNA sequencing data reported in this publication have been submitted to the European Nucleotide Archive (ENA). Accession number is listed in the key resources table. Tabula muris data were downloaded from NCBI GEO database (accession number: GSE109774). Original western blot images of the main figures and source data have been deposited on Mendeley at https://doi.org/10.17632/mmz2gznth5.1 and are publicly available at the date of publication. Microscopy data reported in this paper will be shared by the lead contact upon request. This paper does not report original code.

EXPERIMENTAL MODEL AND STUDY PARTICIPANT DETAILS

Animal models
All experiments were approved by the Behörde für Justiz und Verbraucherschutz der Freien und Hansestadt Hamburg, Germany (permit number: N070/2019). All the animal procedures conformed to the Directive 2010/63/EU of the European Parliament on the protection of animals used for scientific purposes. The animals were kept in the breeding facility of the University Medical Center Hamburg-Eppendorf under animal-friendly husbandry conditions in all phases of life. This applies to the space available, group or individual housing and cage enrichment.

Tie2-Cre (B6.Cg-Tg(Tek-cre)1Ywa/J[41] - RRID:IMSR_JAX:008863), Cdh5-CreER^T2 (Tg(Cdh5-cre/ERT2)1Rha[69] - RRID:IMSR_EM:14891), Prox1-CreER^T2 (Tg(Prox1-cre/ERT2)1Tmak[70] - RRID:IMSR_EM:13737) and Pde2a global knockout (B6; 129P2-Pde2A < tm1Dgen>/H; EM: 02366[25] - RRID:IMSR_EM:02366) mouse lines were previously described. ES cell line containing 'knockout-first' Pde2a allele (Pde2a^tm1a(EUCOMM)Wtsi) was obtained from The European Conditional Mouse Mutagenesis Program (EUCOMM). After obtaining germ line transmission, LacZ-neo cassette was removed by crossing with a FLPe deleter strain[71] followed by mating to C57BL/6J for at least five generations.

Pde2a; Tie2-Cre
Breeding pairs of Pde2a^fl/fl female and Pde2a^fl/+;Tie2-Cre male mice were used to generate Pde2a^fl/+; Tie2-Cre and littermate Pde2a^fl/fl control embryos.

Pde2a; Cdh5-CreER^T2
Breeding pairs of Pde2a^fl/fl female and Pde2a^fl/fl; Cdh5-CreER^T2 male mice were used to generate Pde2a^fl/fl; Cdh5-CreER^T2 and littermate Pde2a^fl/fl control embryos.

Pde2a; Prox1-CreER^T2
Breeding pairs of Pde2a^fl/fl male or female and Prox1-CreER^T2 male or female mice were used to generate Pde2a^fl/fl; Cdh5-CreER^T2 and littermate Pde2a^fl/fl pups. All experimental embryos/mice were compared to control embryos/mice from the same litter. All embryos/mice in experiments had equal distributions of both sexes.

Experiments were performed at embryonic day (E) 14.5, E16.5, E17.5 or postnatal day (P) 11, while mouse endothelial cell isolation was performed from organs of 12-weeks-old mice. Mouse genotyping was performed by extracting genomic DNA from tail clip samples using blackPREP Rodent Tail DNA Kit according to the manufacturer's instruction. Samples were genotyped by PCR (primers used for PCR can be found in the key resources table). To induce Cre-mediated recombination in embryos, pregnant females from Pde2a; Cdh5-CreER^T2 line were injected intraperitoneally with 1mg 4-hydroxytamoxifen (stock 10mg/ml in peanut oil) from E10.5 for 4 consecutive days using an Inject®-F syringe. For postnatal induction of Cre-mediated recombination, mice from Pde2a;

Prox1-CreER^{T2} line were injected intraperitoneally with 2μl of 4-hydroxytamoxifen (stock 25μg/μl in 100% ethanol) at P2 and P3 with a Hamilton® syringe. To induce Cre-mediated recombination for mEC isolation, 8-week-old mice from *Pde2a; Cdh5-CreER^{T2}* line were injected intraperitoneally with 1mg tamoxifen (stock 10mg/ml in peanut oil) for 5 consecutive days using an Inject®-F syringe.

Cell culture models

Primary human dermal lymphatic endothelial cells (HDLECs) and human umbilical vein endothelial cells (HUVECs) were obtained from PromoCell. HDLECs are isolated from junvenile forskin and therefore are solely available as male cells. HUVECs are isolated from human umbilical veins and were purchased as a pool from different donors with both sexes.

Cells were seeded on tissue culture-treated dishes coated with 1μg/ml bovine fibronectin diluted in Dulbecco's phosphate buffered saline (referred to as PBS). HDLECs were cultured in complete Endothelial Cell Growth Medium MV2 medium with 25ng/ml of recombinant human VEGF-C and HUVECs were cultured in complete Endothelial Cell Growth Medium. Note, to study PDE2A function *in vitro*, EC monolayer have to be grown to maximum confluency to obtain "tight junctions" with high CLDN5 expression. To obtain 'loose' CLDN5^{Low} junctions, cells were seeded at 65% of standard cell numbers seeded for 'tight' CLDN5^{High} junctions. Murine endothelial cells (mECs) were cultured in mEC medium (0.1% bovine brain extract (BBE)/10% FBS/1%penicillin-streptomycin/1% Non-Essential Amino Acid (NEAA)/Dulbecco Modified Eagle Medium (DMEM). All cells were cultured at 37°C in a humidified atmosphere with 5% CO2 (HDLECs and HUVECs) or 10% CO2 (mECs).

METHOD DETAILS

Murine endothelial cell isolation

mECs were isolated from lung of *Pde2a-flox* controls and *Pde2aflox; Cdh5-CreERT2* mutants as previously described.[78] Three lungs isolated from 12-week-old mice were pooled per genotype. Macrovessels were removed and remaining tissue was thoroughly minced using scissors for 15min. Lung tissue was digested using 1mg/ml Collagenase A (diluted in PBS with 1.25mM CaCl2) in a 37°C water bath for 1.5h, with gentle agitation every 15min. The cell suspension was then passed through a 40μm cell strainer and single cells were pelleted by centrifugation at 300xg for 5min without deceleration. The cell pellet was resuspended in 2mL medium with sheep-anti-rat IgG Dynabeads™ coupled with a CD31 antibody (clone Mec13.3, diluted 1:33). The mix was incubated at 4°C for 45min with constant rotation. Cells coupled to the CD31-Dynabeads™ were positively selected using a DynaMag™-2 washed twice with mEC medium, resuspended in fresh mEC medium and plated on fibronectin-coated culture dishes, as described above. Lung mECs were sorted again once the monolayer has reached confluency. mECs were then processed for microRNA isolation and Western blot analysis.

RNA interference

FlexiTube siRNA was used to knock-down human *PDE2A*. AllStars Negative CTRL siRNA was used as control. Cells were subjected to transfection 24h after plating, using Lipofectamine 3000 according to the manufacturer's instructions.

Cell growth on stiffness hydrogels

24-well Plate Softwell Easy Coat hydrogels of different stiffness (0.1, 1, 2, 4 and 25kPa) were coated with 10μg/ml collagen I rat tail diluted in PBS at 4°C and then at 37°C for 1h each. For some experiments, hydrogels were prepared in-house following the protocol of Tse and Engler.[79] In brief, 0.1M NaOH treated cover slips were silanated with 3-Aminopropyltriethoxysilane and the acrylamide:-bis-acrylamide mixture for the desired stiffness was added to the coverslip. A hydrophobic coverslip (pre-treated with Dichlordimethylsilane) was placed on top to form a flat surface. After 30min polymerization, the hydrophobic coverslip was removed and the hydrogels crosslinked with 0.2mg/ml Sulpho-SANPAH using 365nm UV light. Hydrogels were thoroughly washed with 50mM Hepes pH 8.5 and then incubated with 10μg/ml collagen (diluted in 50mM Hepes pH 8.5) overnight. 0.3x10^5 HDLECs were plated on 12mm diameter hydrogels in a volume of 50μl, allowed to attach at RT for 5min and then at 37°C for 15min, before additional culture medium was added. After 24h culture, cells were fixed with 4% PFA in PBS at RT for a total of 20min, with a change of fixative in between and were then processed for immunofluorescence as described below. For RNA sequencing or Western blot analysis, depending on experiment, 2 or 3 x10^5 cells were plated on 30mm hydrogels in a volume of 100μl. On the day of harvest, cells were incubated in OptiMEM Reduced Serum Medium at 37°C for 30min. OptiMEM was aspirated, cells were carefully washed with PBS and detached from the hydrogels using 0.05% Trypsin/EDTA. Trypsinization was stopped by adding fresh medium after 5min, cells were pelleted by centrifugation at 200xg and RNA or protein isolation was performed as described below.

Bromodeoxyuridine (BrdU) incorporation assay

HDLECs were seeded on fibronectin-coated 6-well plate dishes at 2x10^5 cells per well and transfected with CTRL or *PDE2A* siRNA as described above. The day after transfection, cells were trypsinized and seeded in 8-well Lab-Tek II chamber slides at concentrations of 0.2x10^5, 0.5x10^5 and 1x10^5 cells per well. After 36h ECGMV2 was changed to basal medium (ECGMV2 without supplements) for 4h. Next, 3μg/ml BrdU with 100ng/ml VEGF-C in basal medium were added to the cells for 12h. Subsequently, cells were fixed with 4% PFA in PBS for 20min at RT. Samples were washed once with PBS and incubated with 2N HCL at RT for antigen retrieval for 30min, followed by immunofluorescence analysis.

in vitro permeability assay

To determine paracellular permeability, 0.4×10^5 CTRL or *PDE2A* siRNA treated HDLECs or HUVECs were seeded on fibronectin-coated Transwell filters ($0.4\mu m$ pore size) and grown to confluency. When maximum confluency was reached, 0.25mg/ml FITC-dextran (40kDa) diluted in ECGMV2 was added to the upper chamber of the Transwell filters and monolayer diffusion was allowed for 1h. Fluorescence in the lower chamber was measured with a Tecan Spark® 10M microplate reader, and monolayer integrity was confirmed by immunofluorescence staining for VE-cadherin after each assay.

cAMP and cGMP incubation

1×10^5 HDLECs were seeded per well in a fibronectin-coated 8-well Lab-Tek II chamber slide. After 48h culture, cells were incubated with $250\mu M$ 8-Br-cAMP or $250\mu M$ 8-Br-cGMP for 1h and 48h, respectively. Subsequently, cells were fixed with 4% PFA in PBS at RT for 20min. Samples were washed once with PBS followed by immunofluorescence analysis as described below.

cAMP/cGMP quantification

cAMP and cGMP measurements were performed using Direct cAMP ELISA Kit and Direct cGMP ELISA Kit. In both cases, the acetylated version of the assays was performed. HDLECs and HUVECs were seeded on fibronectin-coated 6-well plates at 2×10^5 cells per well and transfected with CTRL or *PDE2A* siRNA. After 72h, cell pellets were collected, snap frozen and stored at -80°C. To measure cAMP/cGMP, cells were lysed in $300\mu L$ lysis buffer (0.1N HCL/ 0.1% Triton-X100) at RT for 10 min. After centrifugation at 9,500xg for 10 min, $250\mu L$ of samples were transferred to a new tube and processed according to the manufacturer's instructions. Optical density was measured with a Tecan Spark® 10M microplate reader.

Phosphodiesterase activity assay

Cells were homogenized in 20mM Tris-HCl buffer (pH 7.2, 0.2mM EGTA, 5mM β-mercaptoethanol, 2% (v/v) antiprotease cocktail, 1mM PMSF, 5mM $MgCl_2$, 0.1% (v/v) Triton X-100 and centrifuged at 14,000xg for 30 min at 4°C. PDE activity was measured on the supernatant according to the method described by Thompson and Appleman[80] in 60mM Hepes (pH 7.2, 0.1mM EGTA, 5mM $MgCl_2$, 0.5mg/ml bovine serum albumin and 30mg/ml soybean trypsin inhibitor), in a final volume of 0.15ml. The reaction was started by adding tritiated substrate ([3H] cGMP) at a final concentration of $1\mu M$. The reaction was stopped by adding $50\mu l$ of 0.1N HCl and then neutralized with $50\mu l$ of 0.1N NaOH in 0.1M Tris-HCl pH 8.0. Subsequently, $2\mu l$ of 2mg/ml 5'-nucleotidase (snake venom from Crotalus atrox) in 0.1M Tris-HCl pH 8.0 were added. Samples were gently mixed and incubated at 30°C for 30min to allow complete conversion of 5'-nucleotide to its corresponding nucleoside. Unhydrolyzed cyclic nucleotide and the corresponding nucleoside were separated by DEAE-Sephadex A-25 columns. The eluate was mixed with ULTIMA GOLD scintillation liquid (PerkinElmer, USA) and counted on a Tri-Carb 2100TR Liquid Scintillation Counter (2000CA; Packard Instruments, USA). To evaluate the enzymatic activity of PDE2A, the specific inhibitor BAY 60-7550 was added to the reaction mix at a final concentration of $0.1\mu M$.

Notch activity assay

To activate Notch signaling in LECs, 2×10^5 HDLECs per well or 1×10^5 HDLECs per well were seeded on fibronectin-coated 6-well plate dishes or 8-well Lab-Tek II chamber slides respectively, and transfected with CTRL or *PDE2A* siRNA. After 72h, HDLECs were treated twice every 12h with human recombinant soluble DLL4 (sDLL4) ($1\mu g/ml$) for a total of 24h, followed by protein isolation or fixation for immunofluorescence.

To block NOTCH signaling in LECs, 1×10^5 HDLECs per well were seeded on fibronectin coated 8-well Lab-Tek II chamber slide. 72h after plating, HDLECs were incubated for 24h with N-[N-(3,5-Difluorophenacetyl-L-alanyl)]-(S)-phenylglycine t-butyl ester (DAPT) ($5\mu M$) and subsequently processed for immunofluorescence.

p38 inhibition assay

To inhibit phosphorylation of p38 in LECs, 1×10^5 HDLECs per well were seeded on fibronectin-coated 8-well Lab-Tek II chamber slide, transfected with CTRL or *PDE2A* siRNA and, after 72h, treated with p38 inhibitor SB203580 ($10\mu M$) for 24h.

RNA sequencing

RNA sequencing (RNAseq) was performed by BGI, Shenzhen, China. Briefly, mRNA molecules were purified from total RNA using oligo(dT)-attached magnetic beads and fragmented into small pieces using mechanical fragmentation (6min with 85°C). First-strand cDNA was generated using random hexamer-primed reverse transcription, followed by a second-strand cDNA synthesis. The synthesized cDNA was subjected to end-repair and was 3'-adenylated. Adapters were ligated to the ends of the 3'-adenylated cDNA fragments. The adapters were used to amplify cDNA fragments using PCR. PCR products were purified with Ampure XP Beads, and dissolved in elution buffer (EB). The library was validated on the Agilent Technologies 2100 bioanalyzer. Next, the double stranded PCR products were heat-denatured and circularized by the splint oligo sequence. The single strand circle DNA (ssCirDNA) were formatted as the final library. For sequencing, the library was amplified with phi29 DNA polymerase to generate DNA nanoballs (DNB) which had more than 300 copies of one DNA fragment. The DNBs were loaded into the patterned nanoarray and pair end 100 bases reads were generated using sequencing by synthesis.

The quality of the sequence reads was assessed by FastQC (v0.11.9). Trimmomatic (v0.36) was employed to remove sequencing adapters and low-quality bases (Phred quality score below 20) from the 3'-end of the sequence reads.[81] Thereafter, reads were

aligned to the human reference assembly (GRCh38.98) using STAR (v2.7.3a).[74] Batch effect correction was applied with ComBat-seq.[75] Differential expression was assessed with DESeq2,[76] a gene was considered differentially expressed if the corresponding False Discovery Rate (FDR) was lower than or equal to 0.1 and the absolute log2-transformed fold change (log2FC) was higher than or equal to 0.5. The detection of overrepresented pathways was performed using WebGestalt platform 2019.[82]

Immunofluorescence
Mouse tissues
For immunostaining of whole-mount back skins, P11 mesenteries and 100μm vibratome sections, tissues were fixed in 4% PFA or ice-cold Methanol (for CLDN5 analysis) overnight at 4°C, permeabilized in 0.5% Triton-X100/PBS and blocked in 0.3% Triton-X100/PBS (PBSTx)/3% BSA (blocking buffer). Primary antibodies were incubated in blocking buffer at 4°C overnight. After washing in PBSTx, the samples were incubated with Alexa Fluor (AF)-conjugated secondary antibodies in blocking buffer at 4°C overnight. After further washing, the tissue samples were mounted in Fluoroshield Mounting Medium without DAPI. Staining was performed at RT if not specified otherwise. The following antibodies were used: goat antiPROX1 (1:100), rat anti-Endomucin (1:100), rat anti-CD31 (1:100), mouse anti-PDE2A (1:50), goat anti-NRP2 (1:20), goat anti-VEGFR3 (1:100), goat anti-VE-cadherin (1:200), rabbit anti-LYVE1 (1:200), rabbit anti-CLDN5 (1:50), and mouse anti αSMA-cy3 (1:50). Secondary antibodies conjugated to AF488, AF594 and AF647 were obtained from Jackson ImmunoResearch (all used 1:200).
Cells
For immunostaining of HDLECs and HUVECs, cells were seeded in fibronectin–coated 8-well Lab-Tek II chamber slides at the desired concentration (from 0.2x10^5 to 1x10^5 cells per well) and transfected with CTRL or *PDE2A* siRNA as described above. 72h post-transfection, cells were fixed with 4% PFA in PBS at RT for 20min or with ice-cold methanol (for CLDN5 immunostaining) at 4°C for 20min. Samples were permeabilized using 0.5% Triton-X100/PBS for 5min followed by blocking with 2% BSA/PBSTx for 1h. Primary antibodies were incubated for 1h, followed by washing twice with PBSTx and subsequently cells were incubated with secondary antibodies for 45min before further washing and mounting in Fluoroshield Mounting Medium with DAPI. Staining was performed at RT if not specified otherwise. The following antibodies were used: goat anti-PROX1(1:100), mouse anti-PDE2A (1:50), rabbit anti-KI67 (1:200), mouse anti-VE-cadherin (1:100), rabbit anti VE-cadherin (1:100), rabbit anti-CLDN5 (1:50), anti-Cleaved NOTCH1 (1:20), and mouse anti-BrdU (1:2.5 in 3% BSA/PBSTx). Secondary antibodies conjugated to AF488, AF594 and AF647 were obtained from Jackson ImmunoResearch (all used 1:200). Additionally, AF594- or AF488 Phalloidin (1:40) were used. To detect NOTCH1 intracellular domain (NICD) in HDLECs, Alexa Fluor™ 555 Tyramide SuperBoost™ Kit was used according to the manufacturer's instruction.

Immunoprecipitation
4.5x10^5 HDLECs were seeded in 60mm tissue fibronectin-coated culture-treated dishes. After 24h, cells were treated with CTRL or *PDE2A* siRNA as described above. 48h post-transfection EGMV2 medium was changed to basal medium for overnight incubation. The next day at 72h post-transfection, samples were treated with 100ng/mL VEGF-C for 30min, then protein isolation was performed adding 300μL of ice-cold p-Tyr lysis buffer (20mM Tris-HCL pH7.4/150mM NaCl/2mM CaCl_2/1.5mM MgCl_2/1% Triton-x-100/0.04% NaN_3/EDTA-free protease inhibitors)/1mM NaVO_4 per dish. Cell lysates were incubated at 4°C in overhead rotation for 30 min, centrifuged at 14,000xg, 4°C, for 20min. 90μL of the supernatant from each sample was transferred into a new tube (total lysate (TL) samples), while 3μL anti-VEGFR3 antibody (Millipore) + 40μL Protein G Sepharose™ Fast Flow were added to the remaining volume of each sample (immunoprecipitation (IP) samples) and incubated at 4°C in overhead rotation for 2h. IP samples were then centrifuged at 3,000xg, 4°C, for 3min, and the pellet washed three times with 1mL of ice-cold p-Tyr lysis buffer + EDTA-free protease inhibitors + 1mM NaVO_4. Proteins were denatured using 4xLaemmli sample buffer with 10% β-mercaptoethanol for the TL samples or 1xLaemmli sample buffer with 10% β-mercaptoethanol for the IP samples at 95°C for 5min, then processed for Western blot as described below.

Western blot
Total protein extract was obtained adding 200μl ice-cold pTyr lysis buffer (20mM Tris-HCl pH7.4/ 150mM NaCl/ 2mM CaCl_2/ 1.5mM MgCl_2/ 1% Triton-x-100/ 0.04% NaN_3/ EDTA-free protease inhibitors) to the cells plated on fibronectin-coated 6-well plates. Cell lysates were incubated at 4°C in overhead rotation for 30min, then centrifuged to discard cell debris at 14,000xg, 4°C, for 15 min. Supernatants were collected and protein concentration was determined using a Pierce™ BCA Protein Assay Kit according to manufacturer's instructions. Subsequently, equal amounts of proteins were denatured using 4xLaemmli sample buffer with 10% β-mercaptoethanol at 95°C for 5min, then separated via SDS-PAGE. Proteins were transferred to a Immobilion®¯P Transfer Membrane (0.45μm pore size) and blocked for 1h at RT in 1xTris Buffered Saline Tween (TBST) (150mM NaCl/ 10mM Tris-HCl (pH 7.4)/ 0.05% Tween/ 5% (w/v) milk powder). When phosphorylation was analysed, the membrane was blocked with 1xTBST/2% BSA/ 200μM NaVO_4. The membranes were subjected to overnight incubation at 4°C with primary antibodies diluted in 1xTBST/5% BSA. Membranes were rinsed three times with 1xTBST for 10min each and incubated with HRP-conjugated secondary antibodies (diluted in TBST/5% (w/v) milk powder) at RT for 1h. Membranes were rinsed three times with TBST for 10min each and specific binding was detected using the enhanced chemiluminescence (ECL)® Select Western Blotting Detection Reagent and the Gel Doc™ MP Imaging System. Protein molecular masses were estimated relatively to the electrophoretic mobility of co-transferred prestained protein marker PageRuler® Prestained Protein Ladder. The following primary antibodies were used: mouse anti-PDE2A (1:300), rabbit

anti-PDE3A (kind gift of Chen Yan,[77] 1:1000), goat anti-VEcadherin (C19 clone, 1:250), goat anti-VEcadherin (1:1000), rabbit anti-CLDN5 (1:500), mouse anti-VEGFR3 (1:500), mouse anti-phosphotyrosine (4G10 clone, 1:1000), rabbit anti-p38 MAPK (1:1000), rabbit anti-phospho-p38 MAPK (1:1000), rabbit anti-β-actin (1:1000), and goat anti-PROX1 (1:200).

Flow cytometry

Back skins were collected from E14.5 *Pde2a; Tie2-Cre* or E17.5/E18 *Pde2a; Cdh5-CreER^T2* embryos, dissected in ice-cold PBS and then digested with 4mg/ml Collagenase Type IV/ 0.2mg/ml DNase I/10% FBS/PBS (for E17.5 enzyme concentrations were doubled) under constant shaking with 700 rpm at 37°C for 12-15min (E14.5) or 40 mins (E17.5). Samples were filtered using a 70μm nylon filter and then washed twice with FACS buffer (0.5% FBS/2mM EDTA in PBS) to quench enzymatic activity by dilution, before the cell pellet was resuspended in 100μl Fc block (1:100 in FACS buffer) and incubated on ice for 10min. Next, cells were stained with CD31-PE-Cy7 (1:300), PDPN-APC (1:200), CD45-eF450 (1:20), Ter119-eF450 (1:20) and CD11b-eF450 (1:20) on ice for 15min. Dead cells were labelled using 1μM SytoxBlue. Cells were re-filtered and directly subjected to sorting with a BD Biosciences FACSAria™IIIu run with Diva 8.0.1 software. Single cells were gated from FSC-A/FSC-H plots, followed by exclusion of dead cells and immune cells (CD45+/Ter119+/CD11b+). ECs were gated based on CD31 and LECs (CD31+/PDPN+) were collected directly in RLT lysis buffer for RNA isolation. Compensation was achieved using UltraComp eBeads Plus Compensation Beads. If not stated otherwise samples were incubated and handled on ice.

qRT-PCR analysis

For qRT-PCR analysis of HDLECs, HUVECs and mECs, total RNA was isolated by RNeasy® Mini Kit. In case of sorted murine ECs RNAeasy® Micro Kit was used. RNA was reverse transcribed using SuperScript® IV VILO cDNA Synthesis Kit according to the manufacturer's instructions. cDNA from sorted murine ECs was additionally pre-amplified using the TaqMan™ PreAmp Master Mix. Gene expression levels were analyzed using TaqMan™ Gene Expression Assay and a StepOnePlus RT PCR system. Relative gene expression levels were normalized to GAPDH. The following probes were used for human samples: Hs99999905 *GAPDH*, Hs00194509_m1 *DLL1*, Hs00704917_s1 *GJA4*, Hs01577197_m1 *PSEN2*, Hs00159935_m1 *PDE2A*, Hs01012698_m1 *PDE3A*, Hs01098928_m1 *PDE10A*, Hs00698272_m1 *PDE12*, Hs00963643_m1 *PDE4B*, Hs01579625_m1 *PDE4D*, Hs01062025_m1 *PDE6D* and Hs01079617_m1 *PDE8A*. For murine cells, the following probes were used: Mm99999915_g1 *Gapdh*, Mm01136644_m1 *Pde2a* and Mm00468865_m1 *Hey1* and Mm01278617_m1 *Mki67*.

microRNA expression analysis

HDLECs were seeded in fibronectin-coated 6-well plate dishes with 2x10^5 cells per well and transfected with CTRL or *PDE2A* siRNA as described above. At 72h post-transfection, microRNA (miRNA) was isolated using miRNeasy Mini Kit and reverse transcribed using TaqMan™ microRNA Reverse Transcription Kit according to the manufacturer's instructions. miRNA was isolated from lung mECs of *Pde2aflox* controls and *Pde2aflox; Cdh5-CreER^T2* mutants and processed similarly. *miR-139-5p* expression levels were analysed using TaqMan™ microRNA Assay and a TaqMan™ Universal Master Mix II no UNG with a StepOnePlus RT PCR system. Relative microRNA expression levels were normalized to *RNU48* for HDLECs, or *snoRNA202* and *snoRNA234* for mECs.[8] The following probe was used for both sample types: MI0000693 *miR-139-5p*.

Förster resonance energy transfer (FRET) measurements

2x10^5 HDLECs were seeded on 25mm fibronectin-coated glass coverslips. Following 3 days in culture, cells were transduced with an adenoviral vector to express FRET-based biosensor pmEpac1-camps, targeted the plasma membrane,[83] with multiplicity infection of 0.1. After 40 to 48h, cells with sufficient sensor expression were used for FRET measurements performed on inverted fluorescent microscope Leica DMI 3000 B with oil-immersion 63x/1.40 objective and the MicroManager 1.4 software. When quantifying FRET responses, to facilitate better comparison, we calculated the changes of FRET ratio evoked by each drug administration as a % of maximal FRET response evoked by 10μM FSK + 100μM IBMX (a non-selective PDE inhibitor applied at the end of each experiment) which results in positive % max values which reflect cAMP responses. FRET setup included CoolLED at 440nm, beam-splitter DV2 Dual View, and CMOS (OptiMOS, QImaging) camera chip to record images every 10sec. Tested compounds (BAY60-7550, Cilostamid, human Atrial natriuretic peptide (ANP), Isoprenaline) were diluted in FRET buffer (144mM NaCl, 5.4mM KCl, 1mM, MgCl₂, 1mM CaCl₂, 10mM HEPES; pH 7.3). ImageJ was used for the analysis of raw data which were corrected offline in Microsoft Excel as previously described.[84]

Image acquisition

Confocal images of whole-mount back skins, vibratome sections, P11 mesenteries and *in vitro* experiments represent maximum intensity projections of Z-stacks that were acquired using a Leica SP8 inverted microscope with HCX PL APO CS 10x/0.40 DRY or HC PL APO CS2 63x/1.30 GLYC objectives and Leica LAS-X software. Stereomicroscope images of embryos were acquired with Zeiss Stemi 508 with Axiocam 208 Color.

Image quantification

All quantifications were done using Fiji ImageJ unless stated otherwise. For quantification of central actin, a threshold for junctional VE-cadherin staining was applied, a threshold-based mask was created and pixel intensities of the junctional actin fraction and

overall actin pixel intensity was subtracted. For HDLECs, 4–11 images ($250\mu m^2$, maximum intensity projection images with 12 z-stacks) were acquired from n=2 independent experiments. For HUVECs, 5 images ($250\mu m^2$, maximum intensity projection) were acquired from n=3 independent experiments. For junctional CLDN5 immunostaining, pixel intensity measurements, a defined threshold for junctional VE-cadherin staining was applied, a threshold-based mask was created and pixel intensities of CLDN5 immunostaining in the junctions was analysed. CLDN5 pixel intensities (integrated density) were detected from 6 images from n=2 independent experiments. Quantification of proliferating HDLECs was performed by manual counting of KI67+ or BrdU+ cells normalized to the total number of DAPI+ cells per field of view. 4–5 regions for each condition were imaged and quantified from n=5 independent experiments for KI67 staining, n=3 independent experiments for BrdU assay at 0.2×10^5 and 1×10^5 cells per well and n=2 independent experiments for BrdU assay at 0.5×10^5 cells per well. HDLEC numbers per field of view were quantified via DAPI positive cell count of 3-5 images per sample from n=3 independent experiments. Nuclear NICD was quantified within DAPI-positive nuclei from 4-5 regions for each condition and from n=2 independent experiments.

Quantification of lymphatic vessel diameter and avascular midline was done using maximum intensity projection images of tile-scanned E14.5 back skin samples (xy = $4800\mu m$ x $1000\mu m$, upper thoracic region). For measurement of the distance of lymphatic sprouts from the midline (i.e. avascular midline), dorsal midline was marked with a line in the upper thoracic region and 2–4 measurements on each side of the midline were taken from n=16 *Pde2aflox* control embryos and n=13 *Pde2aflox; Tie2-Cre* mutant embryos. Clusters of LECs not connected to the proximal lymphatic network were not taken into account for measurements. Embryonic lymphatic vessel diameter was determined by measuring the thickest part of each vessel segment in between branch points. 20–30 measurements in the upper thoracic region were taken from n=15 *Pde2aflox* control embryos and n=9 *Pde2aflox; Tie2-Cre* mutant embryos. For blood capillary branching measurement in the back skins, midline region without lymphatic vessels was considered (xy = $2000\mu m$ x $860\mu m$) and analysed using the Skeletonize plugin in ImageJ. The final number of branches was calculated as branch points/mm2 in n=10 *Pde2aflox* control embryos and n=8 *Pde2aflox; Tie2-Cre* mutant embryos. Postnatal lymphatic vessel diameter was determined by measuring areas of the central lymphangion part. 21–30 measurements from 3-4 P11 mesenteric collecting vessels were taken from n=2 *Pde2aflox* control embryos and n=2 *Pde2aflox; Prox1-CreER^T2* mutant embryos. The quantification of jugular lymph sac lumen was performed using the ImageJ area measurement plugin with 1-4 measurements per embryo and n=4 *Pde2aflox* control and n=4 *Pde2aflox; Tie2-Cre* mutant embryos. For the classification of lympho-venous valves, n=10 valves from n=8 *Pde2aflox* control embryos and n=6 valves from n=4 *Pde2aflox; Tie2-Cre* mutant embryos were considered. Quantification of VEGFR3 expression was done using maximum intensity projection images of E14.5 back skin samples (4 regions of xy = $1000\mu m$ x $1000\mu m$, upper thoracic region) from n=5 *Pde2aflox* control embryos and n=4 *Pde2aflox; Tie2-Cre* mutant embryos. A threshold was applied to each region and the intensity of VEGFR3 signal was measured and normalized to the area of VEGFR3 signal. For quantifications of PROX1$^+$ cells in E17.5 back skins, 2-3 z-stack images (xy = $2000\mu m$ x $1500\mu m$) per region (midline and maturing plexus) were analysed from n=3 *Pde2aflox* control embryos and n=5 *Pde2aflox; Cdh5-CreER^T2* mutant embryos. A threshold for nuclear PROX1 staining was applied and particle analysis was performed to count positive nuclei. For quantifications of PROX1^{High} valve regions in E17.5 back skins, 1-2 regions of a 2-3 z-stack image (xy = $2900\mu m$ x $1500\mu m$) were analysed from n=3 *Pde2aflox* control embryos and n=5 *Pde2aflox; Cdh5-CreER^T2* mutant embryos. Postnatal lymphatic valve morphology was performed as previously described.[18] 1-4 vascular branches were analysed from n=6 *Pde2aflox* control embryos and n=6 *Pde2aflox; Prox1-CreER^T2* mutant embryos. For quantification of smooth muscle cell (SMC) coverage in postnatal mesenteries, 7-8 areas of 2-4 collecting lymphatic vessels were imaged from n=2 *Pde2aflox* control embryos and n=2 *Pde2aflox; Prox1-CreER^T2* mutant embryos. A threshold was applied to the αSMA signal and the intensity was measured and normalized per area of αSMA signal. Western blot signal quantifications were done using BioRad Image Lab Software or Fiji ImageJ.

RNA single-cell sequencing data analysis

The cellular expression of *Pde2a* in mouse lung tissue was extracted from the publicly available processed data and metadata present in the Tabula Muris data set (deposited on Figshare).[24] The data were normalized using the NormalizeData function as implemented in the Seurat package.[85] The normalized data were autoscaled, and principal component analysis (PCA) was performed on variable genes followed by Uniform Manifold Approximation and Projection (UMAP) visualization (umap package).[72] Clusters were annotated based on literature-curated marker genes of cell phenotypes. The R implementation of the Plotly software (https://plotly.com/r/) was used for violin and dot plot visualization.

QUANTIFICATION AND STATISTICAL ANALYSIS

GraphPad Prism 9 was used for graphic representation and statistical analysis of the data. All means are reported with standard error of the mean (s.e.m.). Two-tailed unpaired Student's *t*-test was used to compare between two means (assuming equal variance) and including Welch's correction (not assuming equal variance). One-sample *t*-test was used to compare sample mean with a normalized control value = 1 or 100. One-way ANOVA with Turkey's or Dunnett's T3 multiple comparison tests were used for comparison of multiple conditions. Sorted murine LECs and BECs mRNA levels were normalized using *GAPDH* as housekeeping gene, $2^{\wedge}(-dCT)$ calculated as a measure of mRNA expression per analysed sample and presented as the percentage of mRNA relative to the average of the (respective) controls. Differences were considered statistically significant when p<0.05. Statistical parameters are found in the figure legends.